



Delft University of Technology

A Morphodynamic Modeling Study on the Formation of the Large-Scale Radial Sand Ridges in the Southern Yellow Sea

Tao, Jianfeng; Wang, Zhengbing ; Zhou, Zeng; Xu, Fan; Zhang, Changkuan; Stive, Marcel

DOI

[10.1029/2018JF004866](https://doi.org/10.1029/2018JF004866)

Publication date

2019

Document Version

Submitted manuscript

Published in

Journal of Geophysical Research: Earth Surface

Citation (APA)

Tao, J., Wang, Z., Zhou, Z., Xu, F., Zhang, C., & Stive, M. (2019). A Morphodynamic Modeling Study on the Formation of the Large-Scale Radial Sand Ridges in the Southern Yellow Sea. *Journal of Geophysical Research: Earth Surface*, 124(7), 1742-1761. <https://doi.org/10.1029/2018JF004866>

Important note

To cite this publication, please use the final published version (if applicable).
Please check the document version above.

Copyright

Other than for strictly personal use, it is not permitted to download, forward or distribute the text or part of it, without the consent of the author(s) and/or copyright holder(s), unless the work is under an open content license such as Creative Commons.

Takedown policy

Please contact us and provide details if you believe this document breaches copyrights.
We will remove access to the work immediately and investigate your claim.

1 **A morphodynamic modeling study on the formation of the large-scale radial sand**
2 **ridges in the Southern Yellow Sea**

3 **Jianfeng Tao^{1,2,3}, Zheng Bing Wang^{2,3,4}, Zeng Zhou^{2,5}, Fan Xu^{2,5,6}, Changkuan Zhang²,**
4 **Marcel J.F. Stive³**

5 ¹State Key Laboratory of Hydrology-Water Resources and Hydraulic Engineering, Hohai
6 University, Nanjing, China

7 ²College of Harbor, Coastal and Offshore Engineering, Hohai University, Nanjing, China

8 ³Faculty of Civil Engineering and Geosciences, Delft University of Technology, Delft, The
9 Netherlands

10 ⁴Deltares, Delft, The Netherlands

11 ⁵School of Environment, The University of Auckland, Auckland, New Zealand

12 ⁶State Key Laboratory of Estuarine and Coastal Research, East China Normal University,
13 Shanghai, China

14
15 Corresponding authors: Dr Zeng Zhou (zeng.zhou@hhu.edu.cn) and Dr Fan Xu
16 (fxu@sklec.ecnu.edu.cn)

17
18 **Key Points:**

- 19 • The fan-shaped morphology of the large-scale radial sand ridges is numerically
20 simulated.
- 21 • The formation of radial sand ridges requires specific conditions primarily characterized
22 by the tidal wave system.
- 23 • The mechanism underlying the asymmetric spatial pattern of the radial sand ridges is
24 revealed.
25

26 Abstract

27 The governing factors underlying the formation of the fan-shaped large-scale radial sand ridges
28 (denoted as “RSRs” hereafter) off the Jiangsu Coast, China, are investigated using an idealized
29 morphodynamic model. A series of simulations are performed to analyze the effects of the M₂
30 tidal constituent along the boundary, the Coriolis forcing, the bed resistance and the sediment
31 availability on the morphodynamic behavior of the RSRs. Numerical results indicate that the
32 tidal regime, characterized by the rotational and progressive tidal wave systems, is dependent on
33 the east coastline of China as well as their specific geographic latitude. Through the comparison
34 between the simulated and the measured morphology, this tidal regime is demonstrated to be the
35 key driver in forming and maintaining the present-day RSRs. The sensitivity runs further suggest
36 that the asymmetric pattern of the RSRs, which shows larger northern sand ridges than the
37 southern ones, results from both the asymmetric distribution of the tidal wave systems and
38 unequal sediment supply. Overall, this study highlights the delicate balance, predominantly
39 represented by the special tidal wave systems and the sediment availability, required to shape the
40 striking large-scale RSRs in the Southern Yellow Sea.

41 **Keywords:** Radial sand ridges; Morphodynamic modeling; Tidal wave systems; Jiangsu Coast;
42 Southern Yellow Sea

43 1 Introduction

44 Sand ridges are geomorphological features widely distributed in estuaries (e.g., the Thames
45 Estuary, Harris, 1988), coastal bays (e.g., the Gulf of Korea, Off, 1963), the ends of straits (e.g.,
46 the Dover Straits, Caston, 1981) and continental shelves (e.g., the North Sea and the East China
47 Sea, Belderson et al., 1982; Stride, 1982; Yang, 1989). The formation of sand ridges favors an
48 environment where abundant sediment is available and the hydrodynamic regime is sufficiently
49 strong to transport sediments (Dyer & Huntley, 1999; Liu & Xia, 1985; Off, 1963; Pattiaratchi &
50 Collins, 1987; Swift, 1975). Most sand ridges around the world are hidden subaqueous
51 landscapes characterized by striking and intricate morphologies, which have received
52 considerable Holocene shelf deposits and/or fluvial sediment supply. These sediments are
53 subsequently reworked by both terrestrial and marine processes, including river inflows (Giosan
54 et al., 2005), wind waves (Hulscher et al., 1993), tidal currents (Van de Meene & Van Rijn,
55 2000a, 2000b), and storm surges (Calvete et al., 2001; Swift, 1975; Trowbridge, 1995).

56 Sand ridges typically exhibit horizontal length scales ranging from several kilometers (mostly in
57 estuaries or river deltas) to hundreds of kilometers (generally on continental shelves), and are
58 characterized by a “wave-length” of several kilometers and an inter-ridge depth of tens of meters
59 (Gao & Collins, 2014). In most cases, the crests of sand ridges are parallel or subparallel to the
60 main tidal current direction (Dyer & Huntley, 1999; Gao & Collins, 2014; Liu & Xia, 1985). At
61 the end of straits or coastal bays where flow diverges or converges, sand ridges often show a
62 fingered or radial planar pattern, such as the sand ridges observed at the Dover Straits (Caston,
63 1981) and the Southern Yellow Sea (Liu et al., 1989).

64 Off (1963) was probably the first to define sand ridges as rhythmic linear sand bodies induced by
65 tidal currents. Since then, the morphological characteristics and the dynamics of sand ridges have
66 attracted a considerable research effort over the last 50 years, particularly on the tidal shelf seas
67 around the UK, and on sand ridges in the North Sea and the Atlantic coast of North America
68 (Caston, 1981; Collins et al., 1995; Dyer & Huntley, 1999; Houbolt, 1968; McBride & Moslow,

69 1991; Swift, 1975). Attention has been given to fundamental theories for the formation and long-
70 term evolution of sand ridges, so that quantitative morphological prediction of sand ridges can be
71 modeled (Dyer & Huntley, 1999). Huthnance (1982a) first derived the wavelength and the
72 orientation of linear sand ridges, which were consistent with observed tidal sand ridges.
73 Huthnance (1982b) further explained that the refraction of tidal currents over a sand ridge could
74 generate a residual flow, which resulted in the convergence of sediment toward the crest of the
75 sand ridge. This theory was further extended to explain other bed forms, such as shoreface-
76 connected ridges (Calvete et al., 2001; Trowbridge, 1995; Walgreen et al., 2002), linear sand
77 ridges (De Vriend, 1990), and long bed waves (Blondeaux et al., 2009). However, these highly
78 schematized models cannot correctly evaluate the development of tidal sand ridges, when
79 perturbations grow large and non-linear processes take over.

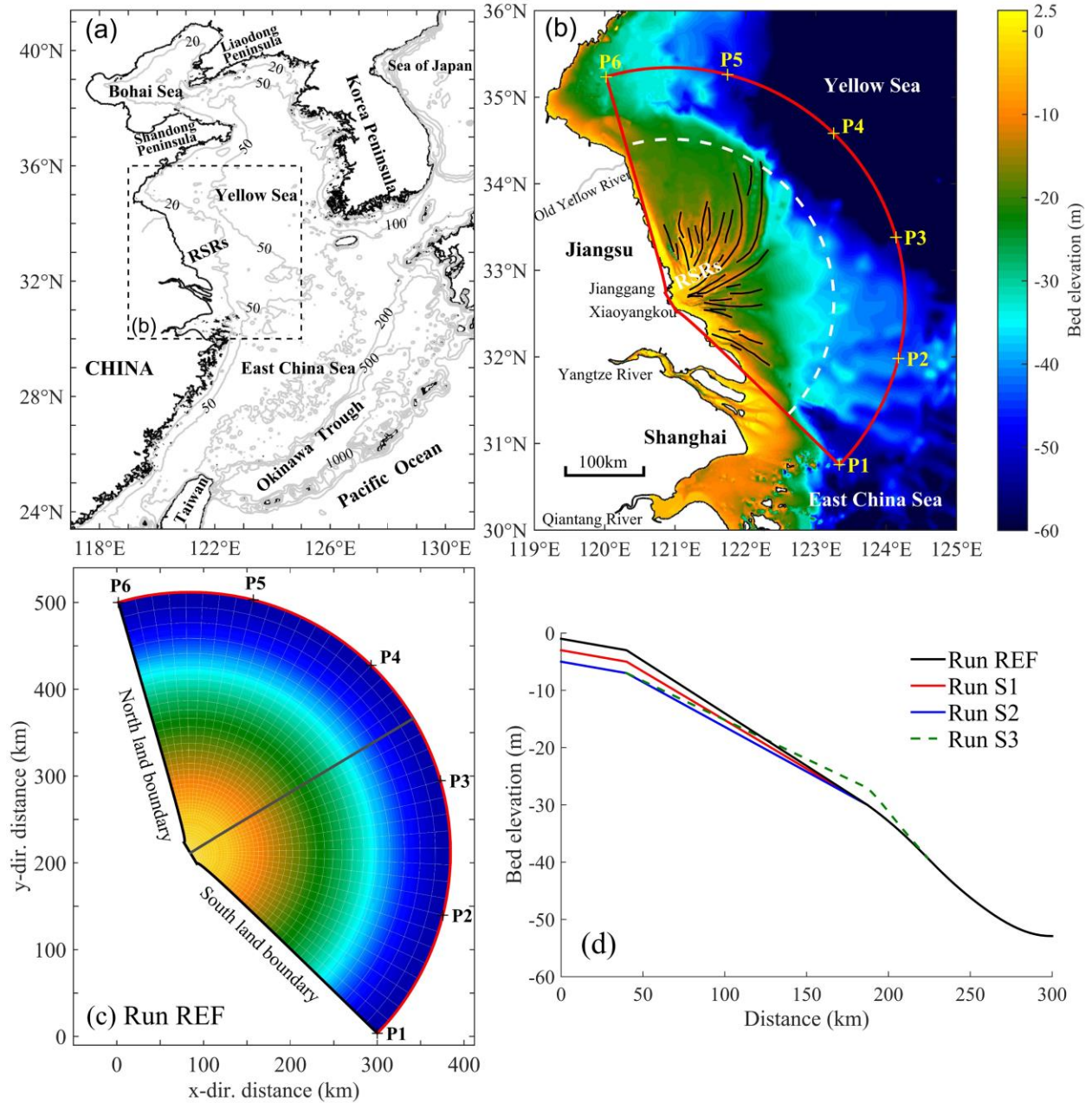
80 Recent advances on long-term morphodynamics by solving the non-linear governing equations
81 numerically (Lesser et al., 2004; Roelvink, 2006; Wang et al., 1995) allow us to simulate the
82 morphodynamic evolution of a system and hence to gain fundamental insights into the ontogeny
83 of coastal landscapes (Zhou et al., 2014c; Zhou et al., 2017). Hibma et al. (2003, 2004) simulated
84 the formation of finite-amplitude tidal sand bars in a long straight tidal basin. Marciano et al.
85 (2005) investigated the channel-shoal patterns in a short tidal basin with both theoretical stability
86 analysis and numerical modeling. These studies indicated that the morphological wavelength is
87 related to the bed slope, the Shields parameter and the sediment availability. Moreover, the
88 Coriolis force has also been found to pronouncedly affect the channel-shoal patterns in estuaries
89 (Schramkowski & De Swart, 2002; Van Leeuwen & De Swart, 2002).

90 The largest sand ridge system along the Chinese coast (Wang et al., 2012b), the radial sand
91 ridges (hereafter referred to as “RSRs”) in the Southern Yellow Sea are morphologically striking
92 because of the remarkable size and radial planar orientation (Figure 1a and 1b). It has been
93 suggested that the RSRs originated from the underlying Holocene strata relict (Li et al., 2001;
94 Wang et al., 1999, 2012b; Yang, 1989) with sediments coming from the neighboring Yangtze
95 River and the Yellow River (Lee & Chough, 1989; Milliman & Meade, 1983; Saito & Yang,
96 1994). The Jiangsu coastline has advanced seaward for about 20-40 km over the last one
97 thousand years, because of the abundant sediment supply (Wang et al., 2012b; Zhang, 1984).
98 After the Yellow River diverted from the Yellow Sea into the Bohai Sea in 1855, part of the
99 sediments of the Old Yellow River Delta were reworked and reformed into the RSRs (Zhou et
100 al., 2014a), which in turn provided natural shelters for the tidal flats behind the offshore sand
101 ridges.

102 Although originating in an earlier environment, sand ridges are dynamic systems which are
103 undergoing modification in response to their present environment, especially the hydraulic
104 regime (Dyer & Huntley, 1999). Many studies have been conducted attempting to elucidate the
105 mechanism underlying the formation of the present-day RSRs (e.g., Du & Wang, 2014; Zhang et
106 al., 1999; Zhu & Chang, 2001). The offshore tidal regime along the Jiangsu Coast have been
107 recognized as the key driven forcing shaping the RSRs, which is supported by two observations:
108 (1) both the tidal current fields and the morphology of the RSRs show similarly radial spatial
109 patterns (e.g., Ren, 1986; Zhang et al., 1999; Zhang, 2012) and (2) several authors found that the
110 radial tidal current patterns can be modeled in the absence of the RSRs (e.g., Qian et al., 2015;
111 Xu et al., 2016; Zhu & Chang, 2001; Zhu & Chen, 2005). The radial tidal current fields are
112 governed by the convergence of a progressive tidal wave from the East China Sea and a local
113 reflected tidal wave formed by the obstruction of the Shandong Peninsula (Zhang et al., 1999;

114 see also Qian et al., 2015; Xu et al., 2016). Other dynamics, such as waves (Xiong et al., 2017)
115 and storm surges (Ren et al., 1985), are considered to be less relevant to the radial morphology of
116 the RSRs, although they can induce considerable short-term sediment transport.

117 The M_2 tidal constituent is dominant in the RSRs (Ren, 1986; Uehara et al., 2002; Zhang, 2012),
118 which has been considered as the major tidal forcing shaping the present-day RSRs (Xing et al.,
119 2012; Xu et al., 2016; Zhang et al., 1999). Previous conclusions about the formation of the RSRs
120 were mainly based on the short-term tidal current fields and the analyses from classical
121 theoretical studies (e.g., Huthnance, 1982a; Off, 1963; Zhang et al., 1999; Zhu & Chang, 2001).
122 Although these indirect proofs are reasonable, a direct evidence lacks to demonstrate the casual
123 relationship between the M_2 constituent and the planimetric shape of the RSRs. In this study, a
124 state-of-the-art morphodynamic model (Delft3D) is employed to investigate the long-term
125 morphodynamic evolution of the RSRs. It is worth noting that this study does not aim to
126 reproduce the exact morphology of the RSRs. We restrict the research questions to: (1) Whether
127 the dominant M_2 tidal constituent can shape the radial planimetric shape of the RSRs or not? (2)
128 How do tidal regime and sediment supply affect the spatial pattern of the RSRs? By resolving
129 these two questions, we intend to gain a more in-depth understanding of the mechanisms
130 underlying the morphodynamics of the RSRs. This morphodynamic study also aims to facilitate
131 further research effort to predict the long-term evolution of the RSRs under threats of sea level
132 rise, reduced sediment supply and increased frequency of coastal storms.



133

134 **Figure 1.** Regional settings of the study area and schematized model configurations. (a)
 135 Bathymetry of the Bohai Sea, the Yellow Sea and the East China Sea. The bathymetric data are
 136 after the gridded bathymetry data of General Bathymetric Chart of the Oceans (GEBCO) with 30
 137 arc-second interval grid; bathymetry contours are given in m. (b) Bathymetry of the Southern
 138 Yellow Sea and the East China Sea. Location indicated by the black dashed box in panel (a).
 139 Bathymetric data were measured in 2006. The black lines roughly denote the sand ridges in
 140 RSRs system. The white dash sector covers the area of the radial sand ridges (RSRs) and is also
 141 the area of morphological change in simulation scenarios. The red lines indicate the schematized
 142 model geometry used in this study. The cross markers (P1 to P6) show the nodes for prescribing
 143 tidal level along the boundary. (c) Plan view of the geometry, grid and bathymetry of the
 144 schematized model. The color bar in panel (c) is the same as that of panel (b). (d) Longitudinal

145 profiles of the bathymetry with different initial bed levels. Location of the longitudinal profile is
146 indicated by the gray line in panel (c). The bed elevation is relative to mean sea level.

147 **2 Study area**

148 The RSRs off the Jiangsu Coast spread on the seabed on the western margin of the Pacific
149 Ocean, where the long, gentle slope of the coastal plains extends offshore towards the semi-
150 enclosed Yellow Sea (Figure 1a). The subaqueous sand ridges stretch more than 200 km from
151 north to south and approximately 140 km from east to west, showing an approximately 150° fan-
152 shaped spatial pattern centered on Jianggang (Xu et al., 2016). The plane scale of each sand ridge
153 is up to 100 km long and 5-10 km wide (Liu et al., 1989), and the water depth in tidal channels
154 can reach 30 m (Wang et al., 2012b). The spatial pattern of the RSRs is asymmetric
155 characterized by northern sand ridges larger than the southern ones (Xu et al., 2016). The bottom
156 sediment of the RSRs mainly consists of fine to very fine sand, with a mean grain size of 2-4 ϕ
157 (Liu et al., 1989; Wang & Ke, 1997) and the sediment mixture is well-sorted (Liu et al., 2012).

158 The tide over the sea area of the RSRs is semi-diurnal with a mean tidal range of 4-6 m (Zhang et
159 al., 1999). The tidal currents tend to be radial in a planar pattern and strong in magnitude, with an
160 average spring tidal current depth-average velocity being 1.5-2.0 m/s and a maximum tidal
161 current velocity of over 2.5 m/s (Wang et al., 2012b). Under normal conditions, wave energy
162 progressively decreases when crossing the RSRs so that wave heights of 7-9 m in the open sea
163 are reduced to approximately 0.4 m at the coast. Under extreme wind conditions, although large
164 waves with a wave height of 2 m can occasionally be observed, the probability is only 5% (Wang
165 et al., 2012b). According to the meteorological record from 1949 to 2007, only 5 of the 76
166 typhoons landed on the Jiangsu Coast or the Yangtze Estuary (Xu et al., 2016).

167 Figure 2 shows the co-tidal chart and tidal current ellipses of the M_2 constituent. The area of the
168 RSRs is influenced by two tidal wave systems, including the progressive tidal wave system from
169 the East China Sea and the anti-clockwise rotational tidal wave system characterized by an
170 amphidromic point approximately 220 km to the north of Jianggang (Figure 2a). These two tidal
171 wave systems converge along the Jiangsu Coast, resulting in an approximately stationary tidal
172 wave, of which the phase difference between the current velocity and tidal level is about 90°
173 over the central RSRs (Li et al., 2001; Tao et al., 2018; Xu et al., 2016; Zhang et al., 1999). Both
174 the magnitudes of the current velocities and the tidal amplitudes peak in the central RSRs, due to
175 the convergence of the two tidal wave systems. The tidal current fields in the RSRs show a radial
176 in planar pattern centered in Jianggang (Figure 2b), which is consistent with the fan-shaped
177 morphology of the RSRs (e.g., Tao et al., 2018; Xu et al., 2016). The tidal current ellipses show a
178 bidirectional flow in the north and a rotational flow in the south over the RSRs.

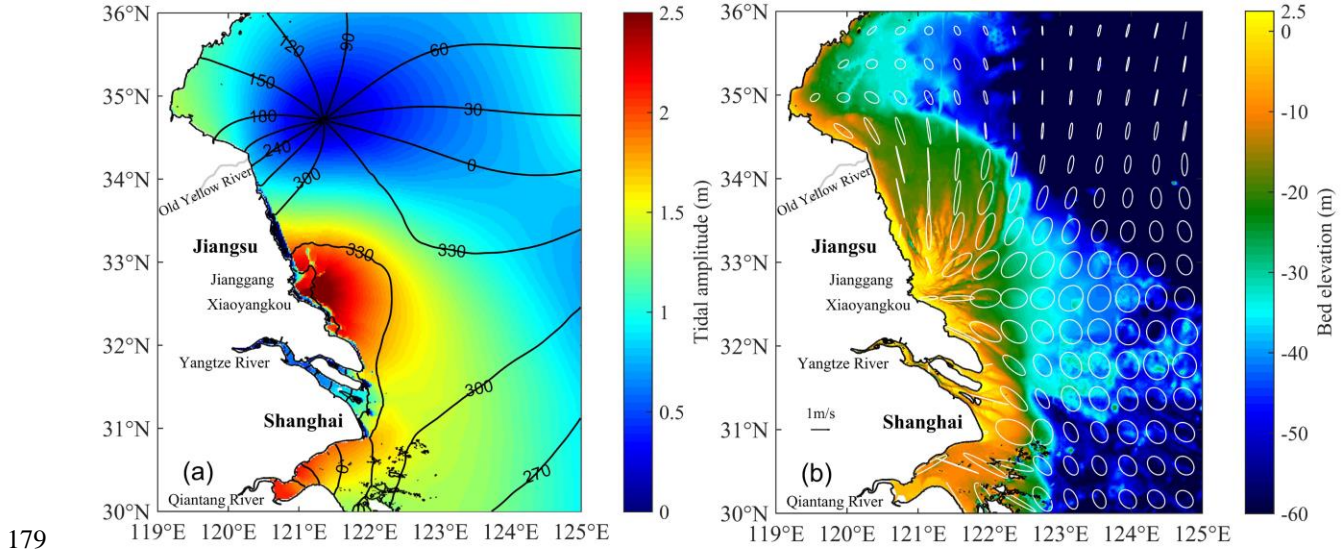


Figure 2. (a) Co-tidal chart and (b) tidal current ellipses of the M_2 constituent in the Southern Yellow Sea (modified after Tao et al., 2018). The color code in panel (a) indicates tidal amplitudes with black co-phase lines in degrees. The color code in panel (b) shows the bed elevation of the Southern Yellow Sea.

184 3 Methodology

185 3.1 Numerical model

186 An open-source morphodynamic model (Delft3D) is employed in the present study (Lesser et al.,
187 2004). Since the model has been described in detail elsewhere (e.g., Van der Wegen & Roelvink,
188 2008), the governing equations are not introduced herein. The numerical model solves the non-
189 linear 2-D shallow water equations resulting in a detailed description of the flow field (i.e., water
190 levels and velocities) over the model domain. The water level and the velocity fields are then
191 utilized to calculate the sediment transport and the resultant bed evolution.

192 The sediment transport rate is calculated based on the local instantaneous flow condition using
193 the widely-adopted formula of Engelund and Hansen (1967), which accounts for both bed load
194 and suspended load (following e.g., Marciano et al., 2005; Van der Wegen & Roelvink, 2008;
195 Van Maanen et al., 2013):

$$196 \quad S = \frac{0.05U^5}{\sqrt{g}C^3\Delta^2D_{50}} \quad (1)$$

197 where, S is the sediment transport flux (m^2/s), U is the magnitude of depth-average flow velocity
198 (m/s), g is the acceleration of gravity (m/s^2), $C = H^{1/6}/n$ is the Chézy friction coefficient
199 ($\text{m}^{1/2}/\text{s}$), H is the water depth (m), n is the Manning coefficient ($\text{s}/\text{m}^{1/3}$), Δ is the relative density
200 ($(\rho_s - \rho_w)/\rho_w$), ρ_s is the sediment density (kg/m^3), ρ_w is the water density (kg/m^3), and D_{50} is
201 the median grain size (m). Effects of longitudinal and transversal bed slope on the sediment
202 transport are accounted for following Bagnold (1966) and Van Rijn (1993) as described in detail
203 by Van der Wegen and Roelvink (2008). The elevation of the bed is dynamically updated
204 linearly by a morphological factor at each hydrodynamic time step according to mass
205 conservation of sediment (Roelvink, 2006).

206 3.2 Numerical experiments

207 The computational domain is idealized on the basis of the east coast of China, such that the
208 physical implications of different factors can be analyzed in a more straight-forward manner
209 (Figure 1b). The embayment is a fan-shaped area of approximately 150° open angle. The center
210 of the embayment is a 30-km long line segment, which approximates the distance between
211 Jianggang and Xiaoyangkou (Figure 1b). The lengths of the two lateral closed boundaries are
212 both 300 km. The embayment is discretized using an orthogonal curvilinear grid with 200×220
213 cells (Figure 1c). The sizes of the grid cells range from $150 \times 200 \text{ m}^2$ at the landward segment
214 to $3.5 \times 4 \text{ km}^2$ along the seaward arc boundary for the consideration of the balance between the
215 numerical precision and efficiency. The computational time to perform each long-term
216 simulation (up to 2000 years) is approximately two weeks using a 3.7 GHz processor, 8.0 GB
217 RAM personal computer.

218 A reference run (denoted as “REF” hereafter) is designed to reproduce the typical tidal wave
219 system over the RSRs. The tidal amplitudes and the phases of the M_2 constituent at points P1-P6
220 along the seaward boundary are provided by a well-calibrated large-scale tidal wave numerical
221 model according to realistic shoreline and bathymetry (Tao et al., 2009). Other components and
222 their relevant spring-neap tide are not considered, since the M_2 constituent is dominant in the
223 RSRs. The Coriolis Force is calculated based on realistic latitude spatially varying from 30.7°N
224 to 35.2°N (Figure 1b). For the transparency of the idealized model, the initial water depths are
225 set increasing radially from the central landward segment to the seaward boundary (Figure 1c).
226 According to the overall variation of the bed elevation from the land to the sea (Figure 1b), the
227 radial profile consists of a linear sloping upper-flat segment (0.05‰, Wang et al., 2012a), a
228 relatively steep lower-flat one (0.18‰, Wang & Ke, 1997) and a deep-water one gently reducing
229 the slope to zero (Figure 1d). Notice that the present-day RSRs have portions above the mean sea
230 level that are exposed during low tide, but that those are not represented in the initial model
231 bathymetry. The grain size D_{50} is simply unified as $125 \mu\text{m}$. A different value would not affect
232 the simulated morphological patterns when using Engelund and Hansen (1967) formula, as
233 pointed out by many authors (e.g., Dissanayake et al., 2009; Van der Wegen et al., 2008; Zhou et
234 al., 2014c). It can be proved theoretically that only the morphological time scale is changed by
235 changing D_{50} . Other physical parameters, such as the Manning coefficient ($= 0.015 \text{ s/m}^{1/3}$), and
236 the horizontal eddy viscosity coefficient ($= 1 \text{ m}^2/\text{s}$), are set following previous studies (e.g.,
237 Xing et al., 2012; Xu et al., 2016). At the seaward boundary, an “equilibrium boundary
238 condition” technique is employed that the sediment load passing through the boundaries are
239 “perfectly” adapted to the local flow. As a result of considerably large water depths, the erosion
240 or deposition along the seaward boundary is negligible (e.g., Van der Wegen et al., 2008). This
241 technique does not imply that the total amount of sediments is conserved within the
242 computational domain, because sediment fluxes are allowed pass through the boundary.

243 Four sets of additional runs are presented to analyze the effects of the tidal boundary condition
244 (T1-T3), the Coriolis Force (C1-C3), the Manning coefficient (i.e., the bed resistance, R1-R3)
245 and the sediment availability (S1-S3) on the morphodynamics of the RSRs. All the runs are listed
246 in Table 1 varying one model parameterization based on the reference case (run REF). The
247 sediment availability is determined by the initial water depths in runs S1-S3. Arranging
248 according to the initial sediment availability indicates that $\text{REF}=\text{S3} > \text{S1} > \text{S2}$. Notice that varying
249 the initial water depths in runs S1 and S2 are accompanied by changes of bed slopes, which
250 interfere with the analysis on the sediment availability. Therefore, run S3 is designed with a

251 smaller initial bed slope and the same sediment availability compared with run REF. All the runs
 252 are simulated for a 2000-years with the time step of 2 min. Notice that the time scale “2000
 253 years” here is just conceptual for the system to approach a dynamic equilibrium (as argued by
 254 Zhou et al., 2017). Considering the gap in the time scales between hydrodynamic and
 255 morphodynamic processes time scales, the morphodynamic evolution is scaled up linearly by a
 256 morphological factor ($= 200$) (Roelvink, 2006). Typical values of this factor for sandy
 257 environments may range from tens to hundreds (e.g., Dastgheib et al., 2008; Ranasinghe et al.,
 258 2011; Van der Wegen & Roelvink, 2008).

259 **Table 1.** Model configurations, including the tidal boundary conditions, the geometric latitudes
 260 (i.e., testing the Coriolis Force), the Manning coefficients and the initial bed slopes (the blanks
 261 indicate the same parameter as run REF).

Run ID	Tidal boundary							Latitude ($^{\circ}$ N)	Manning coefficient ($\text{s/m}^{1/3}$)	Initial bed slope ($\%$)
	M2 tide	P1	P2	P3	P4	P5	P6			
REF	AMP (m) phase ($^{\circ}$)	1.0 0	1.05 12	0.75 45	0.60 90	0.45 180	1.05 270	real	0.015	0.180
T1	AMP (m) phase ($^{\circ}$)	1.0 0	1.05 54	0.75 108	0.60 162	0.45 216	1.05 270			
T2	AMP (m) phase ($^{\circ}$)	0.75 0	0.75 12	0.75 45	0.75 90	0.75 180	0.75 270			
T3	AMP (m) phase ($^{\circ}$)	0.75 0	0.75 0	0.75 0	0.75 0	0.75 0	0.75 0			
C1								20		
C2								10		
C3								0		
R1									0.010	
R2									0.020	
R3									0.025	
S1										0.167
S2										0.153
S3										0.130

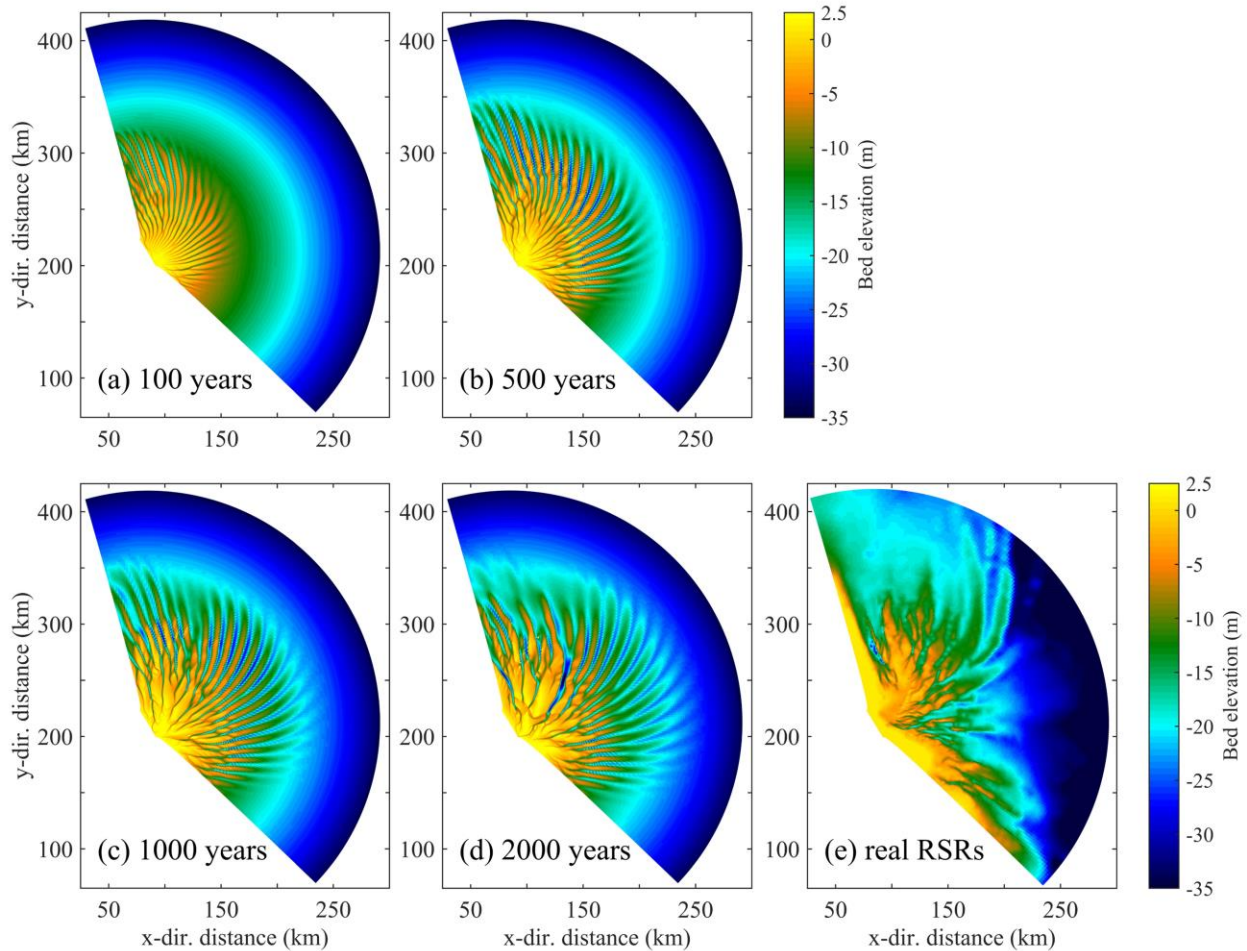
262 Note. “AMP” denotes amplitude; REF is the reference run, of which the simulated
 263 configurations at the end look most like the real RSRs. The “real latitude” means that the latitude
 264 varies spatial depending on the position of the cells in the model (from 30.7° N to 35.2° N). The
 265 “initial bed slope” represents the second part of the profile as shown in Figure 1d.

266 4 Results

267 4.1 The simulated morphodynamic evolution

268 The simulated morphological patterns of run REF at years 100, 500, 1000 and 2000 are shown in
 269 Figure 3. At year 100, a series of thin sand ridges are formed near the landward apex, where the
 270 tidal current velocities are relatively large due to the convergence of the tidal waves. The sand
 271 ridges are elongated in the north and relatively short in the south. This spatial variation in the
 272 length of the sand ridges is related to tidal flow pattern: bidirectional in the north and rotational

273 in the south (Xu et al., 2016), see Figure 2b. Sediments continuously accrete in the central region
 274 of the RSRs and the sand ridges near the apex gradually merge, leading to the formation of
 275 several huge sand bodies (Figure 3b and 3c). At year 2000, the spatial patterns of the sand ridges
 276 tend to be stabilized and show similarly radiated planar forms as the current RSRs.



277

278 **Figure 3.** Morphologies simulated in (a-d) run REF and of (e) the real RSRs.

279 To clarify whether the present system converges to a morphodynamic equilibrium (Zhou et al.,
 280 2017), we quantify the morphodynamic evolution using the mean square root of the overall
 281 variations in bed level relative to the initial state (as e.g., Garnier et al., 2006; Nnafie et al.,
 282 2014):

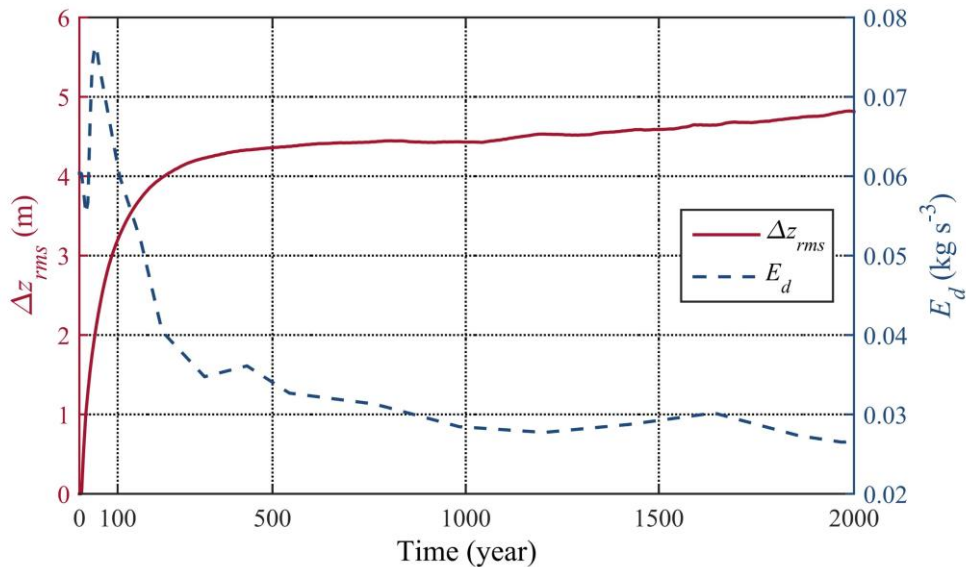
$$283 \quad \Delta z_{rms}(t) = \sqrt{\frac{1}{A} \iint_A [z_t(x, y, t) - z_0(x, y)]^2 dx dy} \quad (2)$$

284 where A is the total planar area of the embayment, and $z_0(x, y)$ and $z_t(x, y, t)$ are the bed
 285 surface elevations at time 0 and t respectively. The morphodynamic evolution can also be
 286 considered as a self-organized process tending to minimize the energy dissipation caused by, for
 287 example, the bed resistance and sediment transport (Rodríguez-Iturbe et al., 1992). The mean

288 energy dissipation is calculated following the expression proposed by Van der Wegen et al.
 289 (2008):

$$290 \quad E_d = \frac{1}{A} \iint_A \left[\left| \rho_w g n^2 \frac{U^3}{\sqrt{H}} \right| + \left| \frac{0.05}{\Delta D_{50}} \rho_w \sqrt{g n^3} \frac{U^5}{\sqrt{H}} \right| \right] dx dy \quad (3)$$

291 The time series of the quantified bed evolution Δz_{rms} and the total energy dissipation E_d over
 292 the 2000-year simulation period are shown in Figure 4. The energy dissipation is relatively high
 293 at the beginning of the simulation, which implies that the initial bed morphology is far away
 294 from the equilibrium configuration (Van der Wegen & Roelvink, 2008; Zhou et al., 2014b,
 295 2014c). Correspondingly, the system experiences pronounced evolution with Δz_{rms} increasing
 296 and E_d decreasing rapidly in the first 200 years. As the radial channel-ridge patterns are formed
 297 between year 100 and 500 (Figure 3a and 3b), the variations of Δz_{rms} and E_d are both reduced,
 298 indicating that the interaction between the tidal flow and the bed topography progressively
 299 becomes milder. Around the year 1500, the variation of Δz_{rms} is minimal and the energy
 300 dissipation E_d maintains at a low level. Therefore, it can be inferred that the system
 301 asymptotically converges to morphodynamic equilibrium.



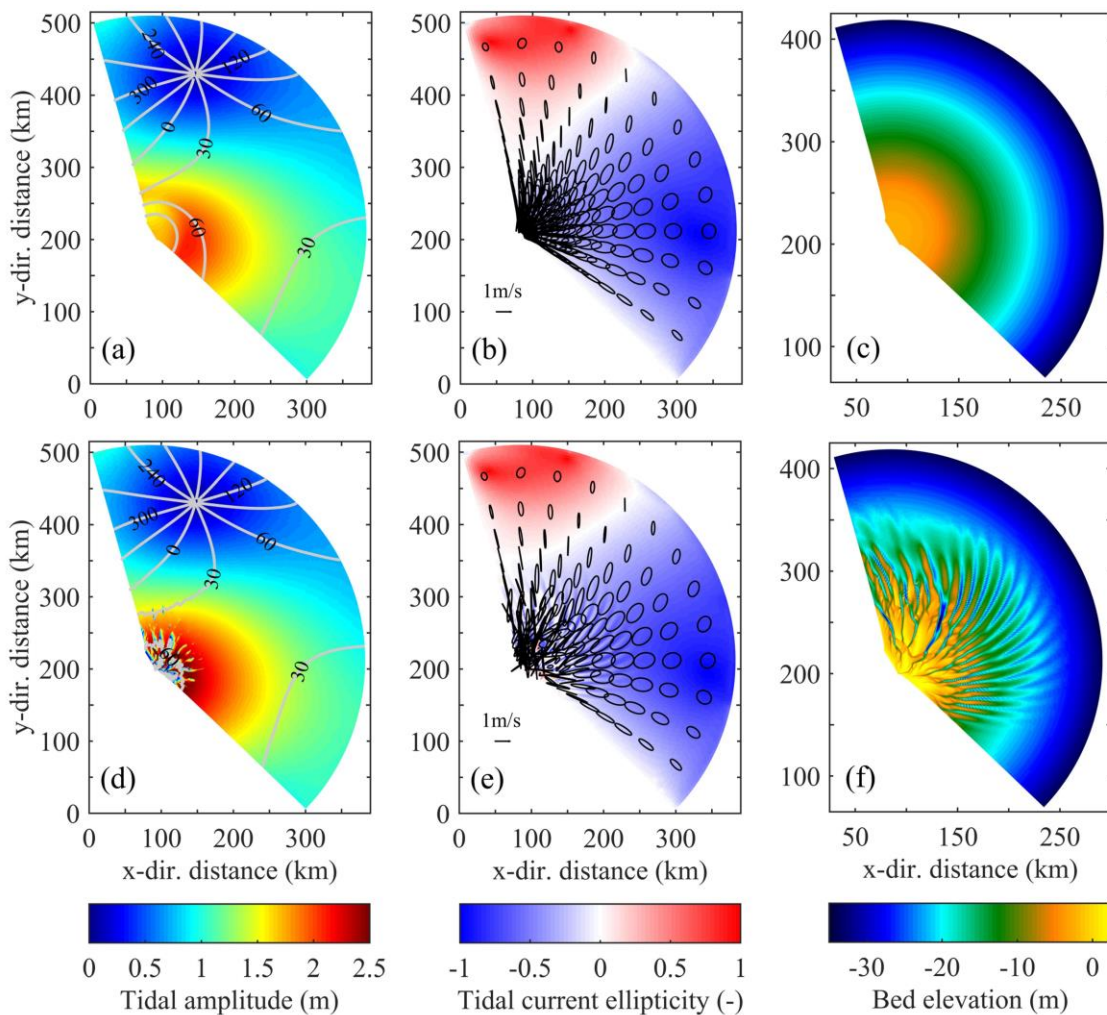
302

303 **Figure 4.** Time series of the overall variation of the Δz_{rms} and the energy dissipation per unit
 304 area E_d averaged over a tidal cycle.

305 4.2 The equilibrium configuration

306 Figure 5a shows the co-tidal chart of the M_2 constituent in run REF calculated using the initial
 307 bathymetry. The model successfully reproduces the typical tidal wave systems, which are
 308 characterized by an amphidromic point located in the north and the convergence of the tidal
 309 waves to the central area (e.g., Zhang et al., 1999). The tidal ellipses show a fan-shaped pattern
 310 with their major axes mainly oriented towards the center of the embayment. Moreover, the
 311 bidirectional and rotational tidal currents respectively occupy the north and south of the
 312 embayment (Figure 5b), which is also consistent with the tidal current fields over the RSRs (e.g.,
 313 Xu et al., 2016). On the other hand, small differences are also observed that the modelled

314 southern ellipses show less elliptical than the real case. This can be attributed to the restriction of
 315 the land boundary, which extends farther seaward than the real coast. The resultant 2000-year
 316 sand ridges show a similarly radiated spatial pattern and planimetric scale as the real RSRs
 317 (comparing Figure 3d with Figure 3e). The sand ridges located in the north are elongated, while
 318 those in the south are relatively short, which correspond to the distribution of the tidal ellipses
 319 (Figure 5b and 5e). The sand ridges are bending anti-clockwise, which is related to the rotations
 320 of the tidal ellipses in the centrifugal direction (Figure 5b). The tidal regime at year 2000
 321 are overall in line with those at year 0 (Figure 5d), while the tidal currents tend to be bidirectional
 322 in the channels even in the south of the RSRs (Figure 5e).

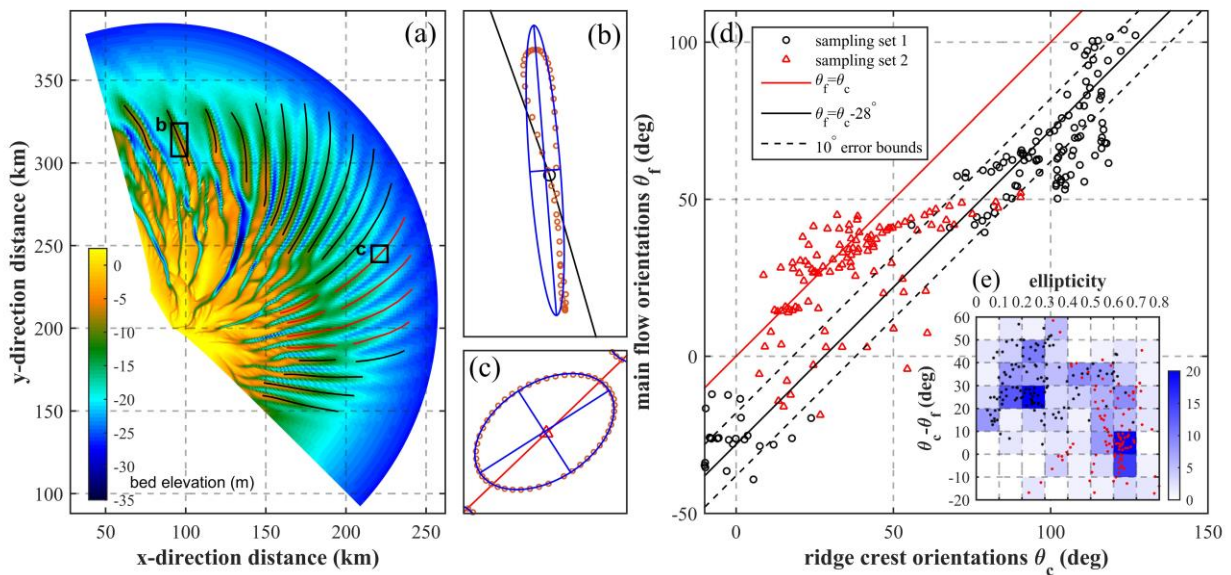


323

324 **Figure 5.** (a) Co-tidal charts and (b) the tidal current ellipses of the M_2 tidal constituent and (c)
 325 the morphology at year 0 simulated in run REF. Panels (d-f) show their 2000-year counterparts.

326 Huthnance (1982a) suggested that an approximately 28° angle between the orientations of
 327 bidirectional tidal current and linear sand ridge crest is necessary to form linear sand ridges. A
 328 series of elongated sand ridges with clear crest lines spreading outside the huge sand bodies are
 329 analyzed (Figure 6a). A least squares method is applied to fit the best ellipses to the tidal vector

330 trajectories and their long axes are used as the main directions of the tidal currents (Figure 6b
 331 and 6c). The local orientations between the tidal current (denoted as “ θ_f ”) and the sand ridge
 332 crest (denoted as “ θ_c ”) are compared in Figure 6d (10 points are sampled on each crest). The
 333 sand ridge crests mainly fall into two groups characterized by $\theta_f \approx \theta_c - 28^\circ$ (red triangles) and
 334 $\theta_f \approx \theta_c$ (black circles) respectively. The spatial distribution of these two types of sand ridge
 335 crests is shown in Figure 6a. Both relationships are also observed in numerical studies which
 336 focus on the tidal current in the RSRs (e.g., Xu et al., 2016). The sand ridge crests following $\theta_f \approx$
 337 $\theta_c - 28^\circ$ mainly locate in the north and the south end of the embayment (see the black lines in
 338 Figure 6a), where bidirectional tidal currents prevail. The other ones indicating $\theta_f \approx \theta_c$ are
 339 situated in the mid-south part (see the red lines in Figure 6a), which are dominated by rotational
 340 tidal currents. Figure 6e shows the distribution of the sampling points in an angle-ellipticity
 341 plane, in which the color code indicates the number of points within an elementary area (i.e.,
 342 density). The angle $\theta_c - \theta_f$ overall shows a decrease tendency with the increase of the ellipticity.
 343 Moreover, the sampling points concentrate in two regions: (1) $20 < \theta_c - \theta_f < 30$ and $0 < E <$
 344 0.3 (E denotes the ellipticity), which indicates bidirectional tidal currents; and (2) $-10 < \theta_c -$
 345 $\theta_f < 10$ and $0.6 < E < 0.7$, which represents rotational tidal currents. Notice that the
 346 orientations of the sand ridge crests are in fact difficult to be exactly identified, since the
 347 morphology is complicated and the top of the sand ridges is flat. This may result in the relatively
 348 scattered distribution of sampling points in Figure 6d and 6e.

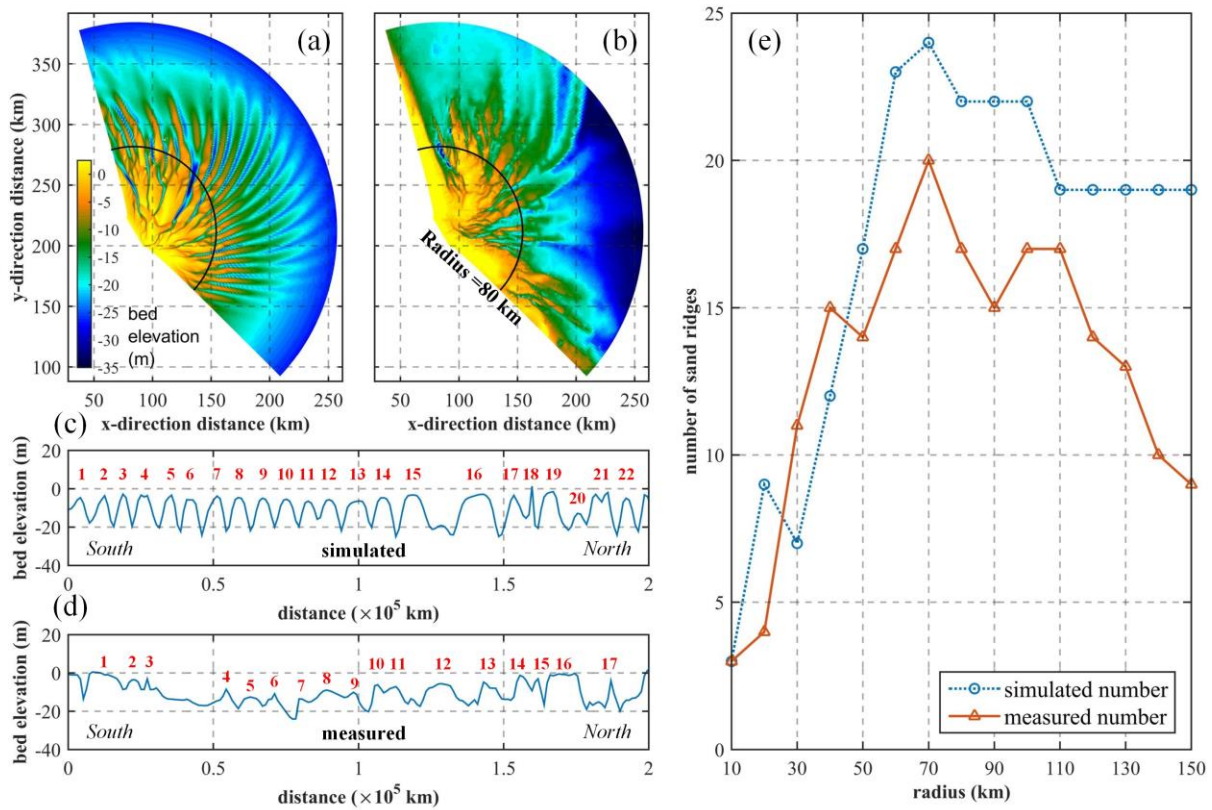


349

350 **Figure 6.** Comparison between orientations of the sand ridges and the main directions of the
 351 tidal currents simulated in run REF. Panel (a) indicates the locations of the sampled sand ridge
 352 crests, on each 10 points are sampled. Panels (b-c) illustrate the main directions of the tidal
 353 currents (red circles) based on the best fitting oval. The main directions of the tidal currents are
 354 approximated by the long axes of the ovals. Panel (d) compares the orientations of the sand
 355 ridges θ_c and the main directions of the tidal currents θ_f . The crests as well as the associated
 356 sampling points, which show consistency with $\theta_f = \theta_c - 28^\circ$ (as suggested by Huthnance,
 357 1982a), are marked in black. The rest ones are marked in red, which indicate $\theta_f = \theta_c$. The black
 358 dashed lines represent the 10° error bounds. Panel (e) shows the distribution of all sampling

359 points in an angle-ellipticity plane. The color code shows the number of points within the range
 360 (i.e., density).

361 To further evaluate the performance of the numerical model, the numbers of sand ridges
 362 simulated in run REF are compared with the real RSRs. The sand ridges are counted along 15
 363 radial sections centered on the apex with radiuses increasing from 10 to 150 km (Figure 7). The
 364 total number of the sand ridges is overestimated by the numerical model, especially in the
 365 seaward sections (radius larger than 110 km), where the total number does not decrease as
 366 significantly as the real RSRs. It can be hypothesized that the sediment availability is excessive
 367 in the model and that sand ridges can extend longer than the real ones. However, the overall
 368 variation tendency is consistent with the real RSRs such that the total number initially increases
 369 and then decreases, peaking at approximately 70 km (Figure 7e).



370

371 **Figure 7.** Comparison in the sand ridge numbers between run REF and the real RSRs. (a) The
 372 2000-year bathymetry simulated in run REF. (b) The measured bathymetry of the RSRs. (c-d)
 373 The bed elevations and the correspondent sand ridge numbers at the cross-section with the radius
 374 of 80 km (see the black arc line in panel (a-b)). (e) The sand ridge numbers at 15 cross-sections
 375 with the radius varying from 10 km to 150 km.

376 4.3 Sensitivity analysis of key parameters

377 In addition to the reference simulation examining the correspondence between the tidal regime
 378 and the radial morphology of the RSRs, four sets of numerical experiments are performed to
 379 analyze the effects of the tidal boundary conditions (runs T1-T3), the Coriolis Force (runs C1-

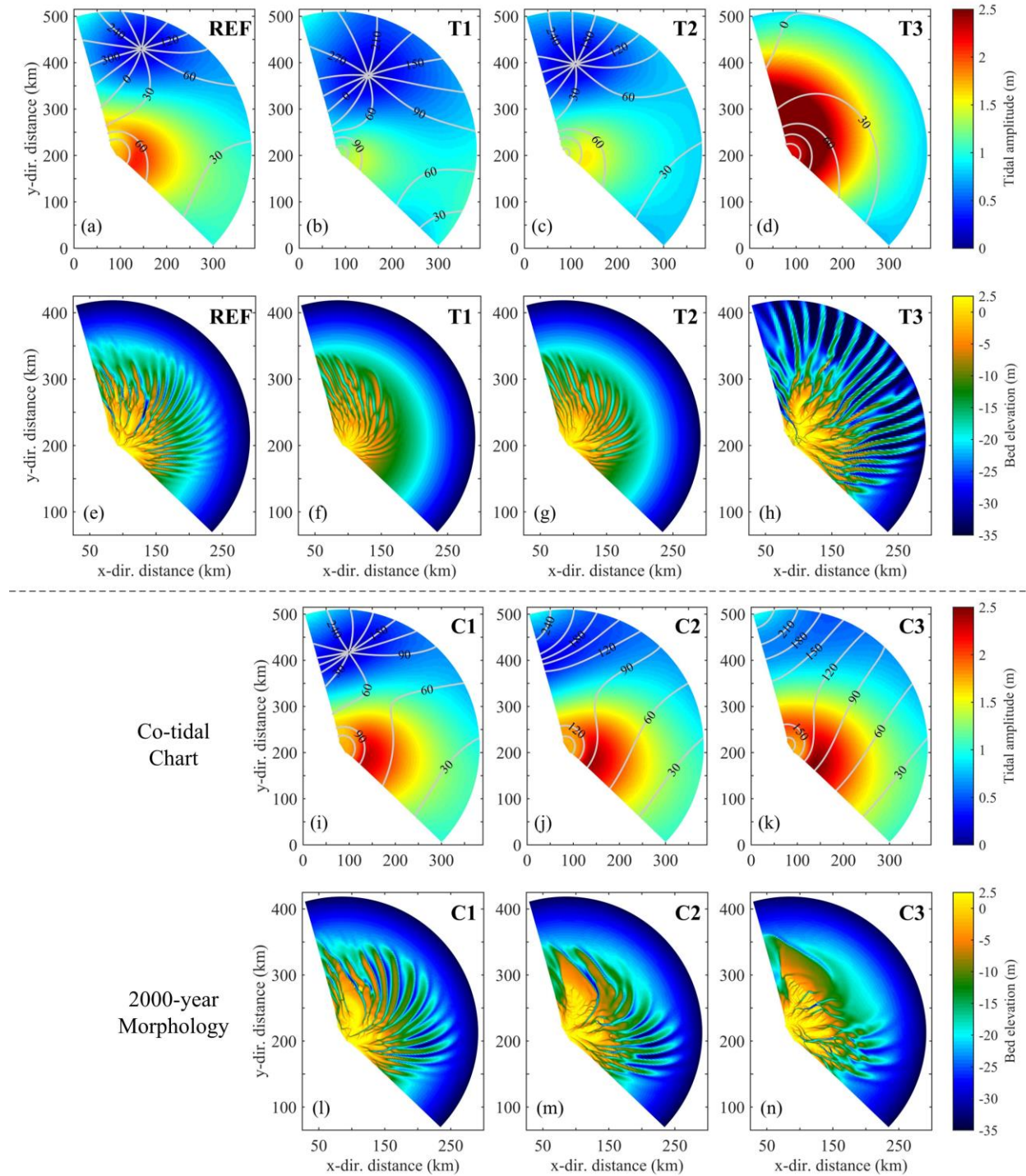
380 C3), the bed resistance (runs R1-R3) and the sediment availability (runs S1-S3) on the tidal
381 regime and the morphology of the RSRs.

382 The tidal phase is modified linearly varying from 0° to 270° along the seaward boundary in run
383 T1. The amphidromic point moves close to the central area, so that the tidal amplitude is reduced
384 (Figure 8b). Correspondingly, the sand ridges are not well developed and the overall scale of the
385 morphological pattern is reduced (Figure 8f). In run T2 with constant amplitude along the
386 seaward boundary and the same phase lag as run REF, similar phenomena are observed: the tidal
387 wave is less concentrated and the overall sand ridges are not well developed (Figure 8c and 8g).
388 The tidal wave directly converges to the center of the embayment in run T3, since both the tidal
389 amplitude and phase are uniform along the boundary (Figure 8d). This leads to the largest tidal
390 amplitudes and the most pronouncedly developed sand ridges among all the scenarios (Figure 8d
391 and 8h). However, these sand ridges are overall radially distributed, while the asymmetric pattern
392 in reality is not reproduced (Figure 8h).

393 The amphidromic point shifts landward as the latitude decreases (i.e., the Coriolis Force
394 decreases, Figure 8i). When the latitude is set 10°N or smaller (i.e., runs C2 and C3, Figure 8j
395 and 8k), the amphidromic point vanishes, such that the tidal wave almost directly propagates
396 across the embayment from south to north rather than converges to the central area. However,
397 without the constraint of the amphidromic point, runs C2 and C3 are of larger tidal amplitude in
398 the central area than run REF. Therefore, huge sand bodies instead of elongated sand ridges are
399 formed in the north of the embayment, which are seemingly more similar as the real morphology
400 of the RSRs (Figure 8m and 8n). It is worth noting that this can be an artefact due to model
401 simplifications. Since the main directions of tidal currents do not orient to the center of the
402 embayment, the sand bodies do not show radial pattern (Figure 8n).

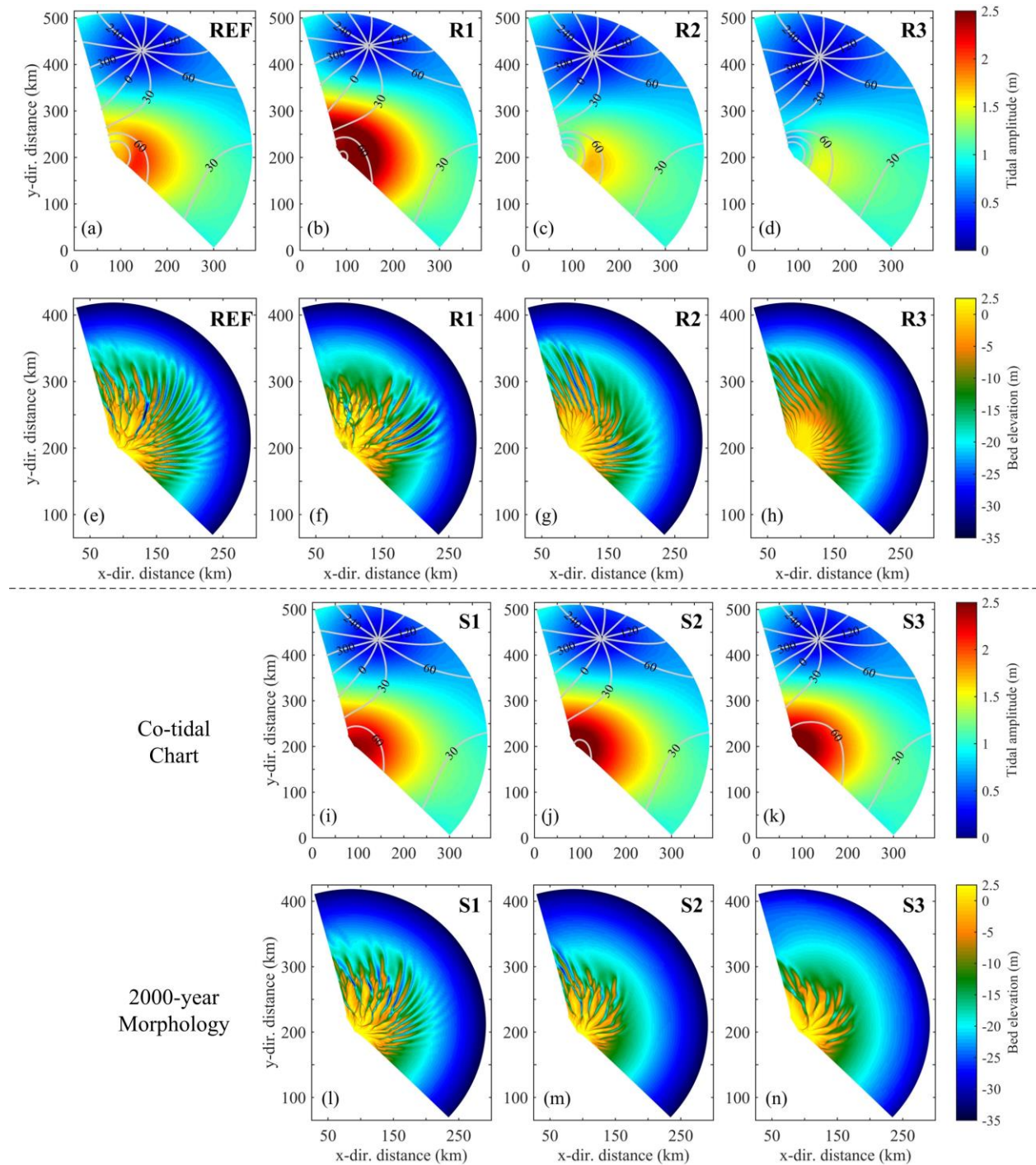
403 An increase in bottom friction leads to decreases in the magnitudes of tidal amplitudes and tidal
404 current velocities, and hence, a decrease in the sediment transport by tidal flow. Correspondingly,
405 runs R2 and R3, which adopt relatively large friction coefficients, indicate smaller sizes of tidal
406 sand ridges than those of run REF (Figure 9g and 9h). Moreover, varying the friction coefficient
407 changes the location of the amphidromic point (Figure 9a-9d), such that the overall tidal wave
408 system and its associated tidal current fields are affected. This further lead to several different
409 characteristics of the sand ridges from run REF, such as the orientation and the bending (Figure
410 9e-9h). Notice that the Manning coefficient used in run R3 ($0.025 \text{ s/m}^{1/3}$) is a common value
411 adopted in coastal areas (e.g., Soulsby, 1997). However, much less and smaller sand ridges are
412 reproduced. This leads to a hypothesis that the reduction of the hydraulic drag due to high
413 sediment concentration is relevant for the formation of the RSRs (e.g., the drag reduction
414 suggested by e.g., Winterwerp & Wang, 2013; Winterwerp et al., 2013).

415 Runs S1 and S2 indicate that both the sizes and the number of the simulated sand ridges decrease
416 as the initial water depth increases (Figure 9l and 9m). This is consistent with the theory
417 proposed by Off (1963) that the development of sand ridges favors abundant sediment
418 availability. Run S3 also show smaller and less sand ridges than run REF (Figure 9n), even
419 though their initial sediment availabilities are the same. Notice that the only difference between
420 these two runs is that the initial bed slope of run S3 is smaller than run REF.



421

422 **Figure 8.** Comparison between run REF and runs T1-T3 and C1-C3 (Latitude = 20, 10, and 0
 423 °N) on the co-tidal charts of the M_2 tidal constituent and the resultant morphologies at year 2000.
 424 The reader is referred to Table 1 for detailed model setup.



425

426 **Figure 9.** Comparison between run REF and runs R1-R3 (Manning coefficient = 0.01, 0.02 and
 427 0.025 s/m^{1/3}) and S1-S3 (initial slope = 0.167, 0.153 and 0.13 ‰) on the co-tidal charts of the M₂
 428 tidal constituent and the resultant morphologies at year 2000. The reader is referred to Table 1
 429 for detailed model setup.

430 **5 Discussion**

431 5.1 Tidal regime, sediment availability and morphology

432 It has been suggested that the formation of the rotational tidal wave system in the north of the
433 RSRs results from the constraint by the east coastline of China, such as the reflection of the tidal
434 waves by Shandong Peninsula (Zhang et al., 1999). The constraint by the coastlines is not
435 explicitly considered, but implicitly represented by the tidal boundary conditions in the present
436 model (Figure 1b). As shown in runs T1 and T2, modifying the phases or the amplitudes along
437 the seaward boundary shifts the position of the amphidromic point and further result in limited
438 development of sand ridges. Moreover, the magnitude of the Coriolis Force, which is determined
439 by the geographic latitude, also considerably affects the tidal wave systems and the formation of
440 linear sand ridges (runs C1-C3, see Figure 8). Therefore, both the current tidal regime and the
441 morphology of the RSRs depend on the east coastline of China as well as their specific
442 geographic latitude.

443 Off (1963) suggested that the formation of sand ridges requires abundant sediment availability
444 and strong current velocities. The effects of these two factors are represented in runs R1-R3 and
445 S1-S3. The sediment transport capability of the tidal current is low in the runs with relatively
446 large Manning coefficient (i.e., runs R2 and R3). Therefore, the resultant morphology indicates
447 that both the development of sand ridges and the accretion of sediment in the central area are
448 limited (Figure 9g and 9h). When simulating with low sediment availability (i.e., runs S1 and
449 S2), large sand bodies are formed in the central area (Figure 9m and 9n), which is attributed to
450 the convergence of the sediments driven by the tidal regime. However, the seaward extension of
451 the sand ridges is limited. The comparison between runs S3 and REF further suggests that the
452 sediments from outer sea is less efficient than those near the coast in forming of the RSRs. This
453 result highlights the contribution of the littoral sediment transport to the development of the
454 RSRs, such as the sediment supply from the Abandoned Yellow River Delta (as suggested by
455 Wang et al., 2012b; Du, et al., 2018).

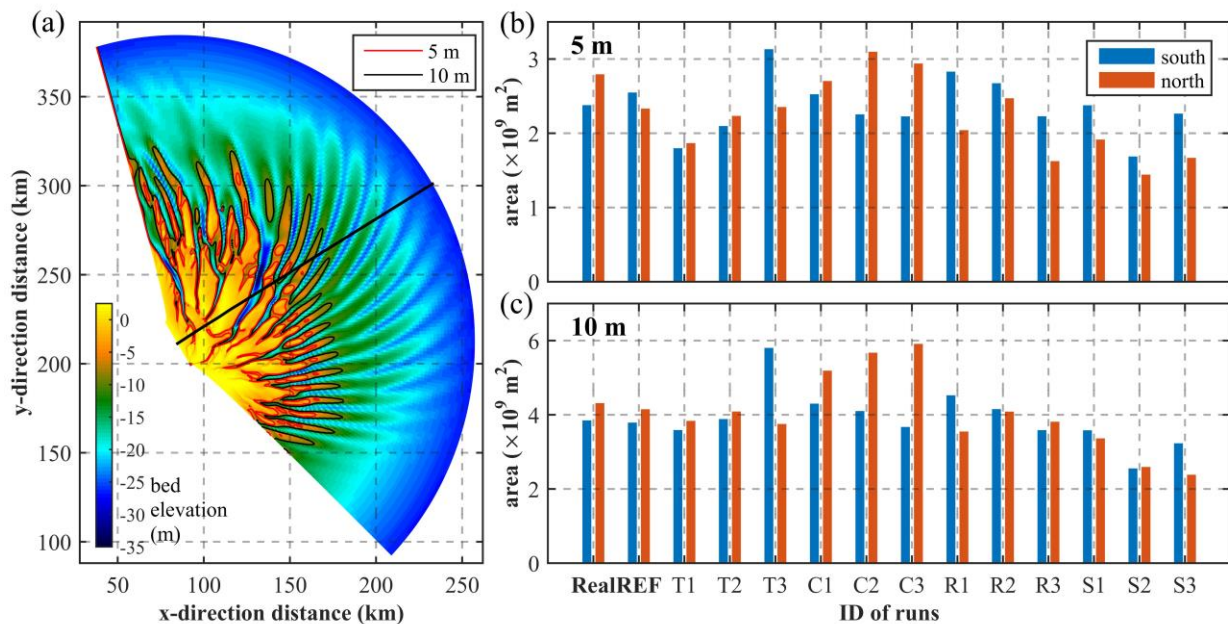
456 5.2 The asymmetric pattern of the RSRs

457 One of the typical characteristics of the RSRs is their asymmetric pattern showing larger
458 northern sand ridges than the southern ones (Xu et al., 2016). Therefore, we are motivated to
459 divide the computational domain into two halves from the middle radial line (see the black bold
460 line in Figure 10a) and compare the planar areas of the sand ridges between the northern and
461 southern parts (Figure 10b and 10c). We calculate the areas of the regions with water depth
462 smaller than 5 m and 10 m respectively, for the consideration of the underwater sand ridges (see
463 black and red contour lines in Figure 10a). The 10-m areas of run REF indicate a favorable
464 distribution consistent with the real RSRs. Moreover, both the 5-m and the 10-m areas of run
465 REF agree well with the real RSRs in magnitude. On the other hand, most sensitivity runs exhibit
466 less consistency with the real RSRs, which highlights the rationality of the parameterizations
467 selected in the run REF.

468 The major sediment source for the present-day RSRs came from the Abandoned Yellow River
469 Delta in the north (Wang et al., 2012b; Du, et al., 2018). However, run REF starts from equally
470 distributed sediment availability between the south and the north. As a result, the 5-m area of run
471 REF appears to be smaller in the north than that in the south, which is inconsistent with the real
472 RSRs. It thus can be inferred that the larger size of the northern sand ridges over the southern

473 ones is partly attributed to the unequal sediment supply between the south and north. On the
 474 other hand, the consistency indicated by the distribution of the 10-m area of run REF confirms
 475 that the tidal regime over the RSRs does prefer a larger scale of the northern sand ridges than the
 476 southern ones.

477 When the rotational tidal wave vanishes and hence the entire embayment is dominated by the
 478 progressive tidal wave (run C3, Figure 8k), the advantage in size of the northern area over the
 479 southern one is amplified (Figures 8n, 10b and 10c). It can thus be inferred that the asymmetric
 480 pattern of the RSRs is promoted by the progressive tidal wave system in the south, while is
 481 restricted by the rotational one in the north. However, run C3 does not show elongated sand
 482 ridges as presented in the real RSRs. This implies that the RSRs cannot be formed without the
 483 convergence of the tidal waves to the central region.



484

485 **Figure 10.** Comparison of the sand ridge areas between the real RSRs and the numerical runs.
 486 Panel (a) illustrates the method of calculating the areas of the southern and the northern
 487 sand ridges. The computational domain is divided into southern and northern halves from the middle
 488 radial line (see the black bold line). Panels (b) and (c) illustrate the planar areas enclosed by the
 489 5-m and 10-m contour lines respectively.

490 5.3 Comparison with other sand ridges

491 Sand ridges over the world have a wide variety of forms due to the difference in hydrodynamic
 492 and sediment regimes (Dyer & Huntley, 1999; Off, 1963). However, the growth of sand ridges
 493 always requires mechanisms that drive the sediment flux to converge to the ridge crest and to
 494 diverge from the channels (e.g., Calvete et al., 2001; Huthnance, 1982a, 1982b). In this section,
 495 the mechanisms underlying the formation of the RSRs are compared with two typical categories
 496 of sand ridges, viz. the linear sand ridges (e.g., Hulscher et al., 1993) and the shoreface-
 497 connected sand ridges (e.g., Swift, 1975).

498 The linear sand ridges (also known as “linear sand banks”) generally occur in open shelf seas,
499 where oscillatory tidal currents prevail. The offshore sand ridges lying on the seabed of the North
500 Sea are representative linear sand ridges, of which the dimensions are typically tens of
501 kilometers long, several kilometers broad and tens of meters high, and the directions slightly
502 deviate from the principle axis of the tidal ellipses. It has been shown that linear sand ridges can
503 be formed on a flat seabed under back-and-forth tidal movements and a faster-than-linear
504 sediment transport rate related to the tidal current velocity (Hulscher, 1993; Huthnance, 1982a,
505 1982b). A possible mechanism leading to the positive feedback between the tidal currents and
506 the erodible seabed has been given (Huthnance, 1982a): when the tidal current moves over a
507 sand ridge, which cyclonically rotates with respect to the main current direction, an anticyclonic
508 residual circulation can be formed around the sand ridge by both the Coriolis and frictional
509 torques. Both torques vanish at the ridge crest, such that sediment can be accreted exactly on the
510 ridge crest.

511 The shoreface-connected ridges are usually observed on storm-dominant inner shelves, where net
512 longshore currents are strong. There are significant morphological differences between the
513 storm-induced ridges (i.e., shoreface-connected ridges) and tide-induced ridges (i.e., tidal sand
514 ridges). The spatial sizes of tide-induced ridges are evidently larger than those of the storm-
515 induced ridges. On the other hand, the orientations of the tidal sand ridges are cyclonically
516 rotated with respect to the major directions of the tidal currents, while the orientations of the
517 shoreface-connected ridges are primarily related to the orientations of the coastlines. The
518 formation of the shoreface-connected ridges has been attributed to the presences of the residual
519 longshore currents and the transversal seabed slope in the inner shelf regions. Since the seabed is
520 inclined, the Coriolis and frictional torques do not vanish as in the flat bed case. Therefore, the
521 anticyclonic residual circulation is constrained to the coastlines (Calvete et al., 2001;
522 Trowbridge, 1995).

523 The RSRs have been classified as tide-induced sand ridges formed during Holocene
524 transgression (Wang et al., 1999; Yang, 1989). The stationary tidal wave system covering the
525 South Yellow Sea, which has been suggested to be crucial for the formation of the RSRs, have
526 been demonstrated to exist since the early Holocene (Wang et al., 2012b; Zhang et al., 1999).
527 Although the ends of the RSRs connect to the Jiangsu Coast, which seems to be similar with the
528 shoreface-connected ridges, the hydrodynamic regime and the spatial dimensions of the RSRs
529 apparently differ from those of the shoreface-connected ridges (Wang et al., 2012b).
530 Comparatively, acting as tidal sand ridges, the RSRs represent evidently tidal-sand-ridge
531 characteristics. For example, the orientations of the sand ridges are anti-clockwise deviating from
532 the major directions of the tidal currents (Figure 6) (Huthnance, 1982b), and the sizes of the
533 seaward parts of the sand ridges are in accordance with tidal sand ridges (Wang et al., 1999).

534 On the other hand, the RSRs, which are situated at a semi-open sea area, differ from those tidal
535 sand ridges observed in open sea regions (e.g., the North Sea) remarkably in terms of their fan-
536 shaped spatial patterns and the huge exposed sand bodies in the central region (Figure 1b, see
537 also Wang et al., 2012b). Controlled by both the land boundaries of China and Korea Peninsula
538 and the slope of the South Yellow Sea Shelf, the tidal waves converge to the central region of the
539 RSRs, and further produce the distinct fan-shaped tidal current field covering this region (Qian et
540 al., 2015). Correspondingly, as shown in Figure 3a, the sand ridges which are formed in the early
541 stage of the simulation, are radially distributed with their spacing diminishing landward, rather
542 than approximately parallel to each other (as e.g., North Sea). As the sediments continuously

543 accumulate in the central region owing to the landward residual movements of the sediment
544 (Xing et al., 2012), the channels between the sand ridges are filled up, and hence the landward
545 parts of the sand ridges merge and finally expose above the water surface (Figure 3b-3d).
546 Overall, the RSRs are tide-induced sand ridges, while the morphological details are determined
547 by their specific geographical position and the typically fan-shaped and converging tidal current
548 fields.

549 5.4 Model capability and further research

550 The idealized model used in this study is developed based on the current tidal regime over the
551 RSRs. This can help us to understand the relationship between the present tidal regime and
552 morphology of the RSRs. However, this model does not aim to solve the controversy related to
553 the origin of the RSRs (Li et al., 2001; Wang et al., 1999, 2012b), because the historical
554 transitions of the coastline (e.g., the Jiangsu coastline) and the sediment source (e.g., the
555 migration of the Yellow River mouth) (Wang et al., 2012b) remain elusive. Moreover, the
556 current boundary condition implies no external sediment supply. Therefore, the model cannot be
557 used to explain whether the sediments are from the Yangtze River (Milliman et al., 1986; Wang
558 et al., 2012b) or the Yellow River (Lee & Chough, 1989; Saito & Yang, 1994; Zhou et al.,
559 2014a). In addition to the simplifications related to the idealized modelling configurations,
560 several processes that may play a certain role in shaping the RSRs are neglected and deserve
561 further research:

562 (1) Only non-cohesive sand with a single representative grain size of 125 μm is considered in the
563 model, while the RSRs are characterized by the presence of mixed grain sizes from very fine
564 sand to fine sand (Zhang, 2012). The modelled sand ridges are more irregular than the simulated
565 ones, because of the homogeneous bed sediment configurations used in the present model. On
566 the other hand, processes such as sediment sorting and sand-mud interactions should be
567 addressed in future research, which can play an important role on the morphodynamics evolution
568 of sand ridges (De Swart et al., 2008; Vis-Star et al., 2009).

569 (2) Winds and waves are not considered. Previous studies have shown that waves affect the
570 morphology of sand ridges (Calvete et al., 2002), particularly during low tidal levels (Reynaud et
571 al., 1999). Similarly, storm surges have been found to effectively modify the morphologies of the
572 sand ridges in the short term (Calvete et al., 2001), while tidal currents act as a restoring force in
573 the long term (Zhang et al., 1999).

574 (3) The effect of long-term sea-level rise and riverine sediment supply are not considered in this
575 model, although it has been argued that they played an important role in the evolution of tidal
576 sand ridges (Gao, 2013; Uehara et al., 2002; Uehara & Saito, 2003; Wang et al., 2012b).
577 Sensitivity simulations of Nnafie et al. (2014) indicate that a rising sea-level results in an
578 increasing height of sand ridges. At the same time, their simulated results suggest that sand
579 ridges do not form if the rate of the sea-level rise is too high, or if the initial depth of the inner
580 shelf is too small. On the other hand, major rivers can affect the long-term morphodynamic
581 evolution of the RSRs by favoring sediment deposition and modifying the local morphology near
582 the outlet (Zhou et al., 2014b), which should be properly considered in further research.

583 (4) Extensive human interferences (e.g., the large-scale land reclamations along the Jiangsu
584 Coast) have not been taken into account. According to Song et al. (2013), Tao et al. (2011, 2018),
585 Wang et al. (2012a) and Zhang and Chen (2011), large-scale human activities can modify the

586 tidal wave systems and sediment transport patterns, hence have effects on the morphological
587 development of the RSRs. The fact that these details concerning the hydrodynamic forcing and
588 sediment transport processes can be ignored for simulating the formation of the RSRs and for
589 reproducing their major characteristics reveals that the presented modeling has captured the
590 major controlling factors for the development of the RSRs.

591 The neglected factors and processes also imply that not all the details of the morphology of the
592 RSRs can be reproduced by the model. Albeit the simplified nature, the model can capture the
593 main features of the RSRs and provide insights into the mechanisms underlying the formation of
594 the RSRs.

595 **6 Conclusions**

596 An open source numerical model (Delft3D) is employed to investigate the morphodynamics of
597 the RSRs of the southern Yellow Sea off the Jiangsu Coast, China. The computational domain is
598 schematically fan-shaped and all the runs start from a smooth sloped bathymetry. The following
599 conclusions can be drawn from this study:

600 (1) Close-to-reality sand ridge patterns can be modelled with the configurations consistent with
601 the current tidal regime of the RSRs. The numerical results directly demonstrate that the
602 formation and the maintenance of the current morphology of the RSRs are governed by the
603 specific tidal regime over the southern Yellow Sea.

604 (2) The current distributions of the rotational and progressive tidal wave systems over the RSRs
605 are important and are determined by the east coastline of China (e.g., the reflection of Shandong
606 Peninsula) and the geographic latitudes (i.e., the Coriolis Force) of the RSRs.

607 (3) Deviation in the location of the amphidromic point can reduce the convergence of the tidal
608 waves to the central area of the RSRs, such that the development of the sand ridges is limited.

609 (4) Sediment can accrete to the central area under the control of the current tidal regime, which
610 results in the formation of the large sand bodies of the RSRs. However, the seaward extension of
611 elongated sand ridges is subject to the availability of sediment supply.

612 (5) The asymmetric spatial patterns of the RSRs characterized by larger northern sand ridges
613 than the southern ones are promoted by the progressive tidal waves and restricted by the
614 rotational tidal waves.

615 (6) Insufficient sediment supply is another reason that the southern sand ridges are smaller than
616 the northern ones in the RSRs.

617 **Acknowledgments**

618 This study is supported by the National Natural Science Foundation of China (No. 51620105005,
619 41606104 and 51739005), the National Key Research and Development Program of China (No.
620 2018YFC0407501) and by the Natural Science Foundation of Jiangsu Province (No.
621 BK20160862). The open source code for Delft3D can be downloaded through the website
622 <https://oss.deltares.nl/web/delft3d/>. We highly appreciate three anonymous reviewers and the
623 editors for their constructive comments.

624 **References**

- 625 Bagnold, R. A. (1966). *An approach to the sediment transport problem from general physics*
626 (USGS Professional Paper 422-I). Washington, DC: United States Government Printing Office.
- 627 Belderson, R. H., Johnson, M. A., & Kenyon, N. H. (1982). Bedforms. In A. H. Stride (Eds.),
628 *Offshore Tidal Sands: Processes and Deposits* (pp. 22-57). London: Chapman and Hall.
- 629 Blondeaux, P., De Swart, H. E., & Vittori, G. (2009). Long bed waves in tidal seas: an idealized
630 model. *Journal of Fluid Mechanics*, 636, 485-495. <https://doi.org/10.1017/S0022112009990887>
- 631 Calvete, D., De Swart, H. E., & Falqués, A. (2002). Effect of depth-dependent wave stirring on
632 the final amplitude of shoreface-connected sand ridges. *Continental Shelf Research*, 22, 2763-
633 2776. [https://doi.org/10.1016/S0278-4343\(02\)00125-5](https://doi.org/10.1016/S0278-4343(02)00125-5)
- 634 Calvete, D., Falqués, A., De Swart, H. E., & Walgreen, M. (2001). Modelling the formation of
635 shoreface-connected sand ridges on storm-dominated inner shelves. *Journal of Fluid Mechanics*,
636 441, 169-193. <https://doi.org/10.1017/S0022112001004815>
- 637 Caston, G. F. (1981). Potential gain and loss of sand by some sand banks in the Southern Bight
638 of the North Sea. *Marine Geology*, 41(3-4), 239-250. [https://doi.org/10.1016/0025-
639 3227\(81\)90083-9](https://doi.org/10.1016/0025-3227(81)90083-9)
- 640 Collins, M. B., Shimwell, S. J., Gao, S., Powell, H., Hewitson, C., & Taylor, J. A. (1995). Water
641 and sediment movement in the vicinity of linear sandbanks: the Norfolk Banks, southern North
642 Sea. *Marine Geology*, 123(3-4), 125-142. [https://doi.org/10.1016/0025-3227\(95\)00010-V](https://doi.org/10.1016/0025-3227(95)00010-V)
- 643 Dastgheib, A., Roelvink, J. A., & Wang, Z. B. (2008). Long-term process-based morphological
644 modeling of the Marsdiep Tidal Basin. *Marine Geology*, 256(1-4), 90-100.
645 <https://doi.org/10.1016/j.margeo.2008.10.003>
- 646 De Swart, H. E., Walgreen, M., Calvete, D., & Vis-Star, N. C. (2008). Nonlinear modelling of
647 shoreface-connected ridges: Impact of grain sorting and interventions. *Coastal Engineering*,
648 55(7-8), 642-656. <https://doi.org/10.1016/j.coastaleng.2007.11.007>
- 649 De Vriend, H. J. (1990). Morphological processes in shallow tidal seas. In R. T. Cheng (Eds.),
650 *Residual currents and long-term transport, Coastal and Estuarine Studies* (Vol. 38, pp. 276-301).
651 Washington, DC: American Geophysical Union.
- 652 Dissanayake, D. M. P. K., Roelvink, J. A., Van der Wegen, M. (2009). Modelled channel
653 patterns in a schematized tidal inlet. *Coastal Engineering*, 56(11-12), 1069-1083.
654 <https://doi.org/10.1016/j.coastaleng.2009.08.008>
- 655 Du, J., & Wang, Y. P. (2014). Evolution simulation of radial sand ridges in the southern Yellow
656 Sea. *Journal of Nanjing University (Natural Sciences)*, 50(5), 636-645.
657 <https://doi.org/10.13232/j.cnki.jnju.2014.05.012> (in Chinese with English abstract)
- 658 Du, J., Shi, B., Li, J., & Wang, Y. P. (2018). Muddy coast off Jiangsu, China: physical,
659 ecological, and anthropogenic processes. In X. H. Wang (Eds.), *Sediment dynamics of Chinese
660 muddy coasts and estuaries: physics, biology, and their interactions* (pp. 25-49). San Diego, CA:
661 Academic Press.

- 662 Dyer, K. R., & Huntley, D. A. (1999). The origin, classification and modelling of sand banks and
663 ridges. *Continental Shelf Research*, 19(10), 1285-1330. [https://doi.org/10.1016/S0278-](https://doi.org/10.1016/S0278-4343(99)00028-X)
664 4343(99)00028-X
- 665 Engelund, F., & Hansen, E. (1967). *A monograph on sediment transport in alluvial streams*
666 (Technical Report). Copenhagen, Denmark: Teknisk Forlag.
- 667 Gao, S. (2013). Holocene shelf-coastal sedimentary systems associated with the Changjiang
668 River: An overview. *Acta Oceanologica Sinica*, 32(12), 4-12. [https://doi.org/10.1007/s13131-](https://doi.org/10.1007/s13131-013-0390-5)
669 013-0390-5
- 670 Gao, S., & Collins, M. B. (2014). Holocene sedimentary systems on continental shelves. *Marine*
671 *Geology*, 352, 268-294. <https://doi.org/10.1016/j.margeo.2014.03.021>
- 672 Garnier, R., Calvete, D., Falqués, A., & Caballeria, M. (2006). Generation and nonlinear
673 evolution of shore-oblique/transverse sand bars. *Journal of Fluid Mechanics*, 567, 327-360.
674 <https://doi.org/10.1017/S0022112006002126>
- 675 Giosan, L., Donnelly, J. P., Vespremeanu, E., Bhattacharya, J. P., Olariu, C., & Buonaiuto F. S.
676 (2005). River delta morphodynamics: examples from the Danube Delta. *Society for Sedimentary*
677 *Geology, Special Publications of SEPM*, 83, 393-411. <https://doi.org/10.2110/pec.05.83.0393>
- 678 Harris, P. T. (1988). Large-scale bedforms as indicators of mutually evasive sand transport and
679 the sequential infilling of wide-mouthed estuaries. *Sedimentary Geology*, 57, 273-298.
680 [https://doi.org/10.1016/0037-0738\(88\)90034-6](https://doi.org/10.1016/0037-0738(88)90034-6)
- 681 Hibma, A., Schuttelaars, H. M., & De Vriend, H. J. (2004). Initial formation and long-term
682 evolution of channel-shoal patterns. *Continental Shelf Research*, 24(15), 1637-1650.
683 <https://doi.org/10.1016/j.csr.2004.05.003>
- 684 Hibma, A., Schuttelaars, H. M., & Wang, Z. B. (2003). Comparison of longitudinal equilibrium
685 profiles of estuaries in idealized and process-based models. *Ocean Dynamic*, 53(3), 252-269.
686 <https://doi.org/10.1007/s10236-003-0046-7>
- 687 Houbolt, J. J. H. C. (1968). Recent sediments in the Southern Bight of the North Sea, *Geologie*
688 *en Mijnbouw*, 47(4), 245-273.
- 689 Hulscher, S. J. M. H., De Swart, H. E., & De Vriend, H. J. (1993). The generation of offshore
690 tidal sand banks and sand waves. *Continental Shelf Research*, 13(11), 1183-1204.
691 [https://doi.org/10.1016/0278-4343\(93\)90048-3](https://doi.org/10.1016/0278-4343(93)90048-3)
- 692 Huthnance, J. M. (1982a). On one mechanism forming linear sand banks. *Estuarine, Coastal and*
693 *Shelf Science*, 14(1), 79-99. [https://doi.org/10.1016/S0302-3524\(82\)80068-6](https://doi.org/10.1016/S0302-3524(82)80068-6)
- 694 Huthnance, J. M. (1982b). On the formation of sand banks of finite extent. *Estuarine, Coastal*
695 *and Shelf Science*, 15(13), 277-299. [https://doi.org/10.1016/0272-7714\(82\)90064-6](https://doi.org/10.1016/0272-7714(82)90064-6)
- 696 Lee, H. J., & Chough, S. K. (1989). Sediment distribution, dispersal and budget in the Yellow
697 Sea. *Marine Geology*, 87(2-4), 195-205. [https://doi.org/10.1016/0025-3227\(89\)90061-3](https://doi.org/10.1016/0025-3227(89)90061-3)
- 698 Lesser, G. R., Roelvink, J. A., Van Kester, J. A. T. M., & Stelling, G. S. (2004). Development
699 and validation of a three-dimensional morphological model. *Coastal Engineering*, 51(8-9), 883-
700 915. <https://doi.org/10.1016/j.coastaleng.2004.07.014>

- 701 Li, C. X., Zhang, J. Q., Fan, D. D., & Deng, B. (2001). Holocene regression and the tidal radial
702 sand ridge system formation in the Jiangsu coastal zone, east China. *Marine Geology*, *173*(1-4),
703 97-120. [https://doi.org/10.1016/S0025-3227\(00\)00169-9](https://doi.org/10.1016/S0025-3227(00)00169-9)
- 704 Liu, T., Shi, X., Li, C., & Yang, G. (2012). The reverse sediment transport trend between
705 abandoned Huanghe River (Yellow River) Delta and radial sand ridges along Jiangsu coastline
706 of China — an evidence from grain size analysis. *Acta Oceanologica Sinica*, *31*(6), 83-91.
707 <https://doi.org/10.1007/s13131-012-0255-3>
- 708 Liu, Z., & Xia, D. (1985). A preliminary study of tidal current ridges. *Chinese Journal of*
709 *Oceanology and Limnology*, *3*(1), 118-133. <https://doi.org/10.1007/BF02852909>
- 710 Liu, Z., Huang, Y., & Zhang, Q. (1989). Tidal current ridges in the southwestern Yellow Sea.
711 *Journal of Sedimentary Petrology*, *59*(3), 432-437. <https://doi.org/10.1306/212F8FB7-2B24-11D7-8648000102C1865D>
- 713 Marciano, R., Wang, Z. B., Hibma, A., De Vriend, H. J., & Defina, A. (2005). Modeling of
714 channel patterns in short tidal basins. *Journal of Geophysical Research*, *110*, F01001.
715 <https://doi.org/10.1029/2003JF000092>
- 716 McBride, R. A., & Moslow, T. F. (1991). Origin, evolution, and distribution of shoreface sand
717 ridges, Atlantic inner shelf, U.S.A. *Marine Geology*, *97*(1-2), 57-85.
718 [https://doi.org/10.1016/0025-3227\(91\)90019-Z](https://doi.org/10.1016/0025-3227(91)90019-Z)
- 719 Milliman, J. D., & Meade, R. H. (1983). World-wide delivery of river sediment to the oceans.
720 *The Journal of Geology*, *91*(1), 1-21. <https://doi.org/10.1086/628741>
- 721 Milliman, J. D., Li, F., Zhao, Y., Zheng, T., & Limeburner, R. (1986). Suspended matter regime
722 in the Yellow Sea. *Progress in Oceanography*, *17*(3-4), 215-227. [https://doi.org/10.1016/0079-6611\(86\)90045-5](https://doi.org/10.1016/0079-6611(86)90045-5)
- 724 Nnafie, A., De Swart, H. E., Calvete, D., & Garnier, R. (2014). Effects of sea level rise on the
725 formation and drowning of shoreface-connected sand ridges, a model study. *Continental Shelf*
726 *Research*, *80*, 32-48. <https://doi.org/10.1016/j.csr.2014.02.017>
- 727 Off, T. (1963). Rhythmic linear sand bodies caused by tidal currents. *Bulletin of the American*
728 *Association of Petroleum Geologists*, *47*(2), 324-341. <https://doi.org/10.1306/BC7437D5-16BE-11D7-8645000102C1865D>
- 730 Pattiaratchi, C., & Collins, M. (1987). Mechanisms for linear sandbank formation and
731 maintenance in relation to dynamical oceanographic observations. *Progress in Oceanography*,
732 *19*, 117-176. [https://doi.org/10.1016/0079-6611\(87\)90006-1](https://doi.org/10.1016/0079-6611(87)90006-1)
- 733 Qian, X., Chen, Y., Zhang, C., Pan, Y., & Das, H. (2014). Radial tidal current field in a semi-
734 enclosed rectangular basin: formation and evolution. *Chinese Journal of Oceanology and*
735 *Limnology*, *33*(4), 1085-1099. <http://dx.doi.org/10.1007/s00343-015-4220-9>
- 736 Ranasinghe, R., Swinkels, C., Luijendijk, A., Roelvink, D., Bosboom, J., Stive, M., & Walstra,
737 D. (2011). Morphodynamic upscaling with the MORFAC approach: Dependencies and
738 sensitivities. *Coastal Engineering*, *58*, 806-811. <https://doi.org/10.1016/j.coastaleng.2011.03.010>
- 739 Ren, M. E. (Eds.). (1986). *Comprehensive investigation of the coastal zone and tidal land*
740 *resources of Jiangsu Province*, Beijing: China Ocean Press (in Chinese).

- 741 Ren, M. E., Zhang, R. & Yang, J. (1985). Effect of Typhoon No.8114 on coastal morphology
742 and sedimentation of Jiangsu Province, People's Republic of China. *Journal of Coastal*
743 *Research*, 1(1), 21-28.
- 744 Reynaud, J., Tessier, B., Berné, S., Chamley, H., & Debatist, M. (1999). Tide and wave
745 dynamics on a sand bank from the deep shelf of the Western Channel approaches. *Marine*
746 *Geology*, 161, 339-359. [https://doi.org/10.1016/S0025-3227\(99\)00033-X](https://doi.org/10.1016/S0025-3227(99)00033-X)
- 747 Rodríguez-Iturbe, I., Rinaldo, A., Rigon, R., Bras, R. L., Marani, A., Ijjász-Vásquez, E. (1992).
748 Energy dissipation, runoff production, and the three-dimensional structure of river basins. *Water*
749 *Resources Research*, 28(4), 1095-1103. <https://doi.org/10.1029/91WR03034>
- 750 Roelvink, J. A. (2006). Coastal morphodynamic evolution techniques. *Coastal Engineering*,
751 53(2-3), 277-287. <https://doi.org/10.1016/j.coastaleng.2005.10.015>
- 752 Saito, Y., & Yang, Z. (1994). Historical change of the Huanghe (Yellow River) and its impact on
753 the sediment budget of the East China Sea. In S. Tsunogai, K. Iseki, I. Koike, T. Oba (Eds.),
754 *Global Fluxes of Carbon and Its Related Substances in the Coastal Sea-Ocean-Atmosphere*
755 *System* (pp. 7-12). Yokohama: M & J International.
- 756 Schramkowski, G. P., & De Swart, H. E. (2002). Morphodynamic equilibrium in straight tidal
757 channels: Combined effects of the Coriolis force and external overtides. *Journal of Geophysical*
758 *Research*, 107(C12), 3227. <https://doi.org/10.1029/2000JC000693>
- 759 Song, D., Wang, X. H., Zhu, X., & Bao, X. (2013). Modeling studies of the far-field effects of
760 tidal flat reclamation on tidal dynamics in the East China Seas. *Estuarine, Coastal and Shelf*
761 *Science*, 133, 147-160. <https://doi.org/10.1016/j.ecss.2013.08.023>
- 762 Soulsby, R. (1997). *Dynamics of marine sands: A manual for practical applications*. London:
763 Thomas Telford.
- 764 Stride, A. H. (1982). *Offshore Tidal Sands: Processes and Deposits*. London: Chapman and Hall.
- 765 Swift, D. J. P. (1975). Tidal sand ridges and shoal-retreat massifs. *Marine Geology*, 18(3), 105-
766 133. [https://doi.org/10.1016/0025-3227\(75\)90007-9](https://doi.org/10.1016/0025-3227(75)90007-9)
- 767 Tao, J. F., Yang, T., Xu, F., & Yao, J. (2011). Effect of large scale tidal flat reclamation on
768 hydrodynamic circulation in Jiangsu coastal areas. In J. H.-W. Lee, C.-O. Ng (Eds.), *Asian and*
769 *Pacific Coasts 2011* (pp. 662-669). Singapore: World Scientific.
- 770 Tao, J. F., Zhang, C. K., Yao, J., & Gong, Z. (2009). *Numerical simulation of tides and tidal*
771 *currents in Jiangsu offshore areas, China*. Paper presented at the 19th International Offshore and
772 Polar Engineering Conference, Osaka, Japan, 1243-1247.
- 773 Tao, J., Xu, F., Yao, P., Zhou, Z., & Zhang, C. (2018). The variations of sediment transport
774 patterns in the radial sand ridges along the Jiangsu coast, China over the last 30 years. *Journal of*
775 *Coastal Research*, 85(SI), 216-220. <https://doi.org/10.2112/SI85-044.1>
- 776 Trowbridge, J. H. (1995). A mechanism for the formation and maintenance of shore-oblique
777 sand ridges on storm-dominated shelves. *Journal of Geophysical Research*, 100(C8), 16071-
778 16086. <https://doi.org/10.1029/95JC01589>

- 779 Uehara, K., & Saito, Y. (2003). Late Quaternary evolution of the Yellow/East China Sea tidal
780 regime and its impacts on sediments dispersal and seafloor morphology. *Sedimentary Geology*,
781 *162*(1-2), 25-38. [https://doi.org/10.1016/S0037-0738\(03\)00234-3](https://doi.org/10.1016/S0037-0738(03)00234-3)
- 782 Uehara, K., Saito, Y., & Hori, K. (2002). Paleotidal regime in the Changjiang (Yangtze) Estuary,
783 the East China Sea, and the Yellow Sea at 6 ka and 10 ka estimated from a numerical model.
784 *Marine Geology*, *183*(1-4), 179-192. [https://doi.org/10.1016/S0025-3227\(01\)00255-9](https://doi.org/10.1016/S0025-3227(01)00255-9)
- 785 Van de Meene, J. W. H., & Van Rijn, L. C. (2000a). The shoreface-connected ridges along the
786 central Dutch coast — part 1: field observations. *Continental Shelf Research*, *20*(17), 2295-2323.
787 [https://doi.org/10.1016/S0278-4343\(00\)00048-0](https://doi.org/10.1016/S0278-4343(00)00048-0)
- 788 Van de Meene, J. W. H., & Van Rijn, L. C. (2000b). The shoreface-connected ridges along the
789 central Dutch coast — part 2: morphological modelling. *Continental Shelf Research*, *20*(17),
790 2325-2345. [https://doi.org/10.1016/S0278-4343\(00\)00049-2](https://doi.org/10.1016/S0278-4343(00)00049-2)
- 791 Van der Wegen, M., & Roelvink, J. A. (2008). Long-term morphodynamic evolution of a tidal
792 embayment using a two-dimensional, process-based model. *Journal of Geophysical Research*,
793 *113*, C03016. <https://doi.org/10.1029/2006JC003983>
- 794 Van der Wegen, M., Wang, Z. B., Savenije, H. H. G., & Roelvink, J. A. (2008). Long-term
795 morphodynamic evolution and energy dissipation in a coastal plain, tidal embayment. *Journal of*
796 *Geophysical Research*, *113*, F03001. <https://doi.org/10.1029/2007JF000898>
- 797 Van Leeuwen, S. M., & De Swart, H. E. (2002). Intermediate modelling of tidal inlet systems:
798 spatial asymmetries in flow and mean sediment transport. *Continental Shelf Research*, *22*(11-13),
799 1795-1810. [https://doi.org/10.1016/S0278-4343\(02\)00038-9](https://doi.org/10.1016/S0278-4343(02)00038-9)
- 800 Van Maanen, B., Coco, G., & Bryan, K. R. (2013). Modelling the effects of tidal range and
801 initial bathymetry on the morphological evolution of tidal embayments. *Geomorphology*, *191*,
802 23-34. <https://doi.org/10.1016/j.geomorph.2013.02.023>
- 803 Van Rijn, L. C. (1993). *Principles of Sediment Transport in Rivers, Estuaries and Coastal Seas*.
804 Amsterdam: Aqua Publications.
- 805 Vis-Star, N. C., De Swart, H. E., & Calvete, D. (2009). Effect of wave–bedform feedbacks on
806 the formation of, and grain sorting over shoreface-connected sand ridges. *Ocean Dynamics*, *59*,
807 731-749. <https://doi.org/10.1007/s10236-009-0210-9>
- 808 Walgreen, M., Calvete, D. & De Swart, H. E. (2002). Growth of large-scale bed forms due to
809 storm-driven and tidal currents: a model approach. *Continental Shelf Research*, *22*(18-19), 2777-
810 2793. [https://doi.org/10.1016/S0278-4343\(02\)00126-7](https://doi.org/10.1016/S0278-4343(02)00126-7)
- 811 Wang, X., & Ke, X. (1997). Grain-size characteristics of the extant tidal flat sediments along the
812 Jiangsu coast, China. *Sedimentary Geology*, *112*(1-2), 105-122. [https://doi.org/10.1016/S0037-0738\(97\)00026-2](https://doi.org/10.1016/S0037-0738(97)00026-2)
- 814 Wang, Y. P., Gao, S., Jia, J., Thompson, C. E. L., Gao, J., Yang, Y. (2012a). Sediment transport
815 over an accretional intertidal flat with influences of reclamation, Jiangsu coast, China. *Marine*
816 *Geology*, *291-294*, 132-146. <https://doi.org/10.1016/j.margeo.2011.01.004>
- 817 Wang, Y., Zhang, Y., Zou, X., Zhu, D., & Piper, D. (2012b). The sand ridge field of the South
818 Yellow Sea: Origin by river-sea interaction. *Marine Geology*, *291-294*, 132-146.
819 <https://doi.org/10.1016/j.margeo.2011.01.001>

- 820 Wang, Y., Zhu, D., You, K., Pan, S., Zhu, X., Zou, X., & Zhang, Y. (1999). Evolution of
821 radiative sand ridge field of the South Yellow Sea and its sedimentary characteristics. *Science in*
822 *China, Series D: Earth Sciences*, 42(1), 97-112. <https://doi.org/10.1007/BF02878503>
- 823 Wang, Z. B., Louters, T., & De Vriend, H. J. (1995). Morphodynamic modelling for a tidal inlet
824 in the Wadden Sea. *Marine Geology*, 126(1-4), 289-300. [https://doi.org/10.1016/0025-](https://doi.org/10.1016/0025-3227(95)00083-B)
825 [3227\(95\)00083-B](https://doi.org/10.1016/0025-3227(95)00083-B)
- 826 Winterwerp, J. C., & Wang, Z. B. (2013). Man-induced regime shifts in small estuaries — I:
827 theory. *Ocean Dynamics*, 63(11-12), 1279-1292. <https://doi.org/10.1007/s10236-013-0662-9>
- 828 Winterwerp, J. C., Wang, Z. B., Van Braeckel, A., Van Holland, G., & Kösters, F. (2013). Man-
829 induced regime shifts in small estuaries — II: a comparison of rivers. *Ocean Dynamics*, 63(11-
830 12), 1293-1306. <https://doi.org/10.1007/s10236-013-0663-8>
- 831 Xing, F., Wang, Y. P., & Wang, H. V. (2012). Tidal hydrodynamics and fine-grained sediment
832 transport on the radial sand ridge system in the southern Yellow Sea. *Marine Geology*, 291-294,
833 192-210. <https://doi.org/10.1016/j.margeo.2011.06.006>
- 834 Xiong, J., Wang, X. H., Wang, Y. P., Chen, J., Shi, B., Gao, J., Yang, Y., et al. (2017).
835 Mechanisms of maintaining high suspended sediment concentration over tide-dominated
836 offshore shoals in the southern Yellow Sea. *Estuarine, Coastal and Shelf Science*, 191, 221-233.
837 <https://doi.org/10.1016/j.ecss.2017.04.023>
- 838 Xu, F., Tao, J., Zhou, Z., Coco, G., & Zhang, C. (2016). Mechanisms underlying the regional
839 morphological differences between the northern and southern radial sand ridges along the
840 Jiangsu Coast, China. *Marine Geology*, 371, 1-17.
841 <http://dx.doi.org/10.1016/j.margeo.2015.10.019>
- 842 Yang, C. S. (1989). Active, moribund and buried tidal sand ridges in the East China Sea and the
843 Southern Yellow Sea. *Marine Geology*, 88(1-2), 97-116. [https://doi.org/10.1016/0025-](https://doi.org/10.1016/0025-3227(89)90007-8)
844 [3227\(89\)90007-8](https://doi.org/10.1016/0025-3227(89)90007-8)
- 845 Zhang, C. K. (Eds.). (2012). *Comprehensive investigation and assessment report of Jiangsu*
846 *offshore*. Beijing: China Science Press (in Chinese).
- 847 Zhang, C. K., & Chen, J. (2011). Master plan of tidal flat reclamation along Jiangsu coastal zone.
848 In J. H.-W. Lee, C.-O. Ng (Eds.), *Asian and Pacific Coasts 2011* (pp. 139-146). Singapore:
849 World Scientific.
- 850 Zhang, C., Zhang, D., Zhang, J., & Wang, Z. (1999). Tidal current-induced formation — storm-
851 induced change — tidal current-induced recovery — Interpretation of depositional dynamics of
852 formation and evolution of radial sand ridges on the Yellow Sea seafloor. *Science in China,*
853 *Series D: Earth Sciences*, 42(1), 1-12. <https://doi.org/10.1007/BF02878492>
- 854 Zhang, R. S. (1984). Land-forming history of the Huanghe River delta and coastal plain of north
855 Jiangsu. *Acta Geographica Sinica*, 39(2), 173-184 (in Chinese with English abstract).
- 856 Zhou, L., Liu, J., Saito, Y., Zhang, Z., Chu, H., & Hu, G. (2014a). Coastal erosion as a major
857 sediment supplier to continental shelves: example from the abandoned Old Huanghe (Yellow
858 River) delta. *Continental Shelf Research*, 82, 43-59. <https://doi.org/10.1016/j.csr.2014.03.015>
- 859 Zhou, Z., Coco, G., Jiménez, M., Olabarrieta, M., Van der Wegen, M., & Townend, I. (2014b).
860 Morphodynamics of river-influenced back-barrier tidal basins: The role of landscape and

- 861 hydrodynamic settings. *Water Resources Research*, 50, 9514-9535.
862 <https://doi.org/10.1002/2014WR015891>
- 863 Zhou, Z., Coco, G., Townend, I., Olabarrieta, M., Van der Wegen, M., Gong, Z., D'Alpaos, A.,
864 et al. (2017). Is “Morphodynamic Equilibrium” an oxymoron? *Earth-Science Reviews*, 165, 257-
865 267. <https://doi.org/10.1016/j.earscirev.2016.12.002>
- 866 Zhou, Z., Olabarrieta, M., Stefanon, L., D'Alpaos, A., Carnello, L., & Coco, G. (2014c). A
867 comparative study of physical and numerical modeling of tidal network ontogeny. *Journal of*
868 *Geophysical Research: Earth Surface*, 119, 892-912. <https://doi.org/10.1002/2014JF003092>
- 869 Zhu, Y., & Chang, R. (2001). On the relationships between the radial tidal current field and the
870 radial sand ridges in the southern Yellow Sea: a numerical simulation. *Geo-Marine Letters*,
871 21(2), 59-65. <https://doi.org/10.1007/s003670100073>
- 872 Zhu, Y., & Chen, Q. (2005). On the origin of the radial sand ridges in the Southern Yellow Sea:
873 Results from the modeling of the paleoradial tidal current fields off the Paleo-Yangtze River
874 Estuary and Northern Jiangsu Coast. *Journal of Coastal Research*, 21(6), 1245-1256.
875 <https://doi.org/10.2112/02-0054.1>